日本磁気学会
ISSN 1882-2924
Journal of the Magnetics Society of Japan
Electronic Journal URL: https://www.jstage.jst.go.jp/browse/msjmag

Vol.40 No.1　2016

Journal

Magnetic Recording

Hard and Soft Magnetic Materials

Thin Films, Fine Particles, Multilayers, and Superlattices

INDEX

JOURNAL OF THE MAGNETICS SOCIETY OF JAPAN

Vol.40 No.1 2016

日本磁気学会

ISSN 1882-2924

HP: http://www.magnetics.jp/ e-mail: msj@bj.wakwak.com
Electronic Journal: http://www.jstage.jst.go.jp/browse/msjmag

基礎理論から最先端の応用技術までを網羅的に取り上げ、
磁気に関するすべてが分かる本格的ハンドブック。

2016年
1月
刊行予定

磁気便覧

日本磁気学会　編

B5判・900頁　定価（本体50,000円＋税）　ISBN978-4-621-30014-5

今日の身の回りでは情報機器、家電品、自動車、発電装置など、幅広い分野で磁気、磁性を応用した製品が、便利で快適な社会生活を支えています。本書は学生から、大学や企業で活躍されている研究者、技術者の方々を対象に磁気、磁性に関連する問題解決の利用のために企図した本格的なハンドブック。初学者にも理解し易いよう、基礎から応用、また歴史的な発展から物性データ、最先端の技術まで含めてわかりやすく解説します。

目次

関連図書

応用物理ハンドブック　第2版	応用物理学会　編 B5判・1100頁　定価（本体38,000円＋税）　ISBN978-4-621-04955-6
高圧技術ハンドブック	毛利信男・村田恵三・上床美也・高橋博樹　編 B5判・438頁　定価（本体20,000円＋税）　ISBN978-4-621-07828-0
金属便覧　改訂6版	社団法人　日本金属学会　編 B5判・1,208頁　定価（本体43,000円＋税）　ISBN978-4-621-04745-3
改訂4版　金属データブック	日本金属学会　編／編集委員長　早稲田嘉夫 A5判・624頁　定価（本体20,000円＋税）　ISBN978-4-621-07367-4
レアメタル便覧	足立吟也　監修 B5判・1938頁　定価（本体129,000円＋税）　ISBN978-4-621-08276-8

丸善出版株式会社
〒101−0051 東京都千代田区神田神保町2−17 神田神保町ビル6階　書籍営業部TEL(03)3512−3256 FAX(03)3512−3270
http://pub.maruzen.co.jp/

電気信号用プローバ設置対応　μ-MOKE装置

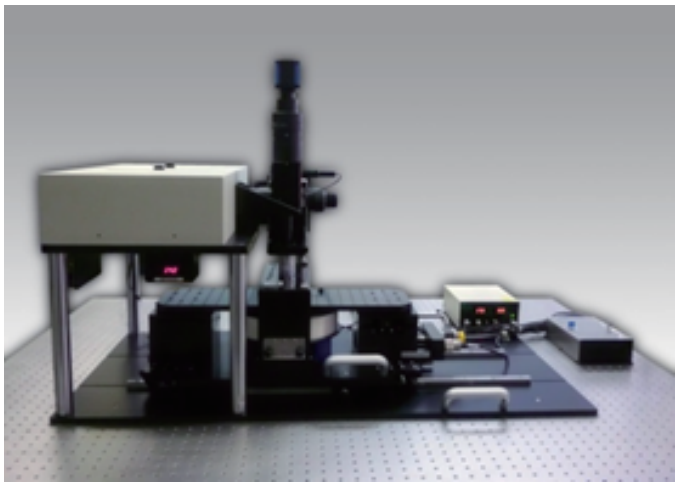

※装置外観は仕様内容や製作上の都合で変更になる場合がございます。

Polar Kerr Hysteresis Loop

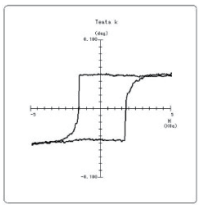

In-Plane Kerr Hysteresis Loop

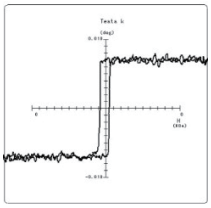

405nm半導体レーザ、及び専用電磁石を用いた、各種磁性材料、主に磁性薄膜を対象とした磁気特性評価用Kerr効果測定装置です。
光源は集光されており、μmオーダの局所領域における磁気特性評価が可能です。光を用いた大気中での高速測定を目的とし、測定のために特別に試料を加工する必要や、特殊な環境を整える必要がなく、簡便に測定を行うことができます。
またステージ部に汎用性を持たせており、電気信号印加用のプローバの設置ができる設計となっています。

測定対象

・各種磁性薄膜・磁性材料
（※表面が鏡面状態にある材料のみ）

主な機能

・ヒステリシスループ作成（Y：θ k-X：H）
・保持力Hc等のパラメータ演算

主な仕様

測定光源：	半導体レーザ（中心波長405nm）	
測定スポット経：	面内（縦）Kerr効果測定	約5μm
	極Kerr効果測定	約2μm
検出感度：	約±0.01°	
電磁石：	面内用電磁石	最大±7kOe
	極用電磁石	最大±10kOe

電気信号用プローバ設置対応　磁区観察装置

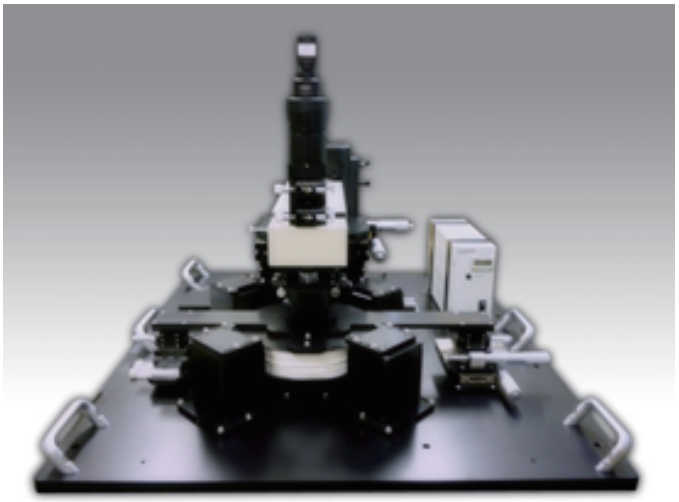

※装置外観は仕様内容や製作上の都合で変更になる場合がございます。

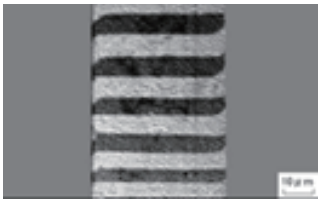

本装置は軟磁性薄膜、珪素鋼板など、その他各種磁性材料の磁区観察を目的とした顕微鏡装置です。
白色光による縦Kerr効果（面内磁区観察）、および極Kerr効果（垂直磁区観察）を利用した非接触かつ迅速・簡便な操作で磁性材料の磁区を観察することができます。また専用電磁石を用いて、発生磁場を制御しつつ、連続して観察画像を取込み動画化するオプションソフトウェアが用意されています。
ステージ部周辺に、電気信号印加用のプローバが設置できる設計となっています。

測定対象

・各種磁性薄膜・磁性材料
（※表面が鏡面状態にある材料のみ）

主な機能

・静止画磁区観察
・連続静止画取込・動画化機能 ※オプション

主な仕様

磁区観察方法：	面内（一軸）方向、極方向	
倍率：	20倍対物レンズ（標準）	※オプションにて50倍対物レンズ等付属可
空間分解能：	約2.5μm	※20倍対物レンズにて
観察範囲：	約250×200μm	
電磁石：	極用電磁石	最大±10kOe
	面内用電磁石	※現在開発中

レーザとレーザ応用システム製品の総合メーカー
NEOARK ネオアーク株式会社
営 業 部／〒156-0041 東京都世田谷区大原2-17-6-108　TEL(03)6379-5539 FAX(03)6379-5688
大阪支店／〒541-0056 大阪市中央区久太郎町2-3-8-201　TEL(06)6271-5123 FAX(06)6271-5110
本社 第1工場・第2工場／八王子市
URL http://www.neoark.co.jp　E-mail:info@neoark.co.jp

世界初！
高温超電導型VSM

新製品

世界初*、高温超電導マグネットをVSMに採用することで
測定速度 当社従来機1/20を実現。
0.5mm cube磁石のBr, HcJ高精度測定が可能と
なりました。
*2014年7月 東英工業調べ

測定結果例

高温超電導VSMによるNdFeB(sint.) 0.5mm cube BHカーブ

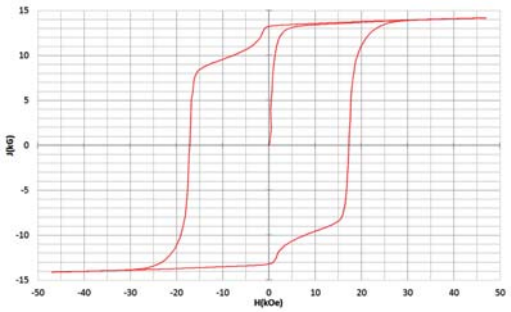

磁化測定レンジ：0.2emu
Br = 13.2kG　　HcJ = 17.2kOe

高温超電導VSMによるNdFeB(sint.) 1mm cube BHカーブ

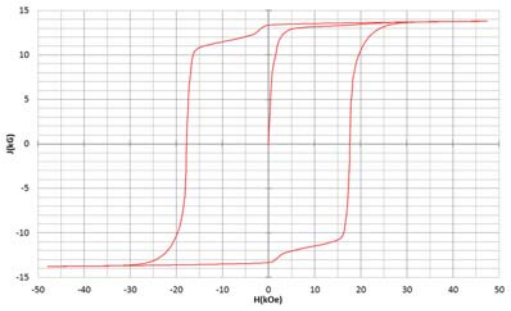

磁化測定レンジ：2emu
Br = 13.3kG　　HcJ = 17.7kOe

高温超電導VSMによるNdFeB(sint.) 4mm cube BHカーブ

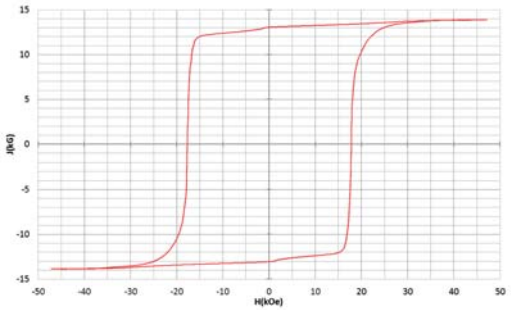

磁化測定レンジ：100emu
Br = 13.1kG　　HcJ = 17.8kOe

高速測定を実現

高温超電導マグネット採用により、高速測定を実現しました。Hmax= 5Tesla, Full Loop 測定が2分で可能です。
（当社従来機：Full Loop測定　40分）

小試料のBr,HcJ高精度測定

0.5mm cube 磁石のBr,HcJ高精度測定ができ、表面改質領域を切り出しBr,HcJの強度分布等、微小変化量の比較測定が可能です。
また、試料の加工劣化の比較測定が可能です。

試料温度可変測定

－50℃～＋200℃温度可変UNIT（オプション）

磁界発生部の小型化

マグネットシステム部寸法：0.8m×0.3m×0.3m

TOEI 東英工業株式会社
http://www.toeikogyo.co.jp
〒194-0035 東京都町田市忠生1-8-13
TEL：042-791-1211　FAX：042-792-0490
E-mail : sales@toeikogyo.co.jp

マルチフィジックスモデル

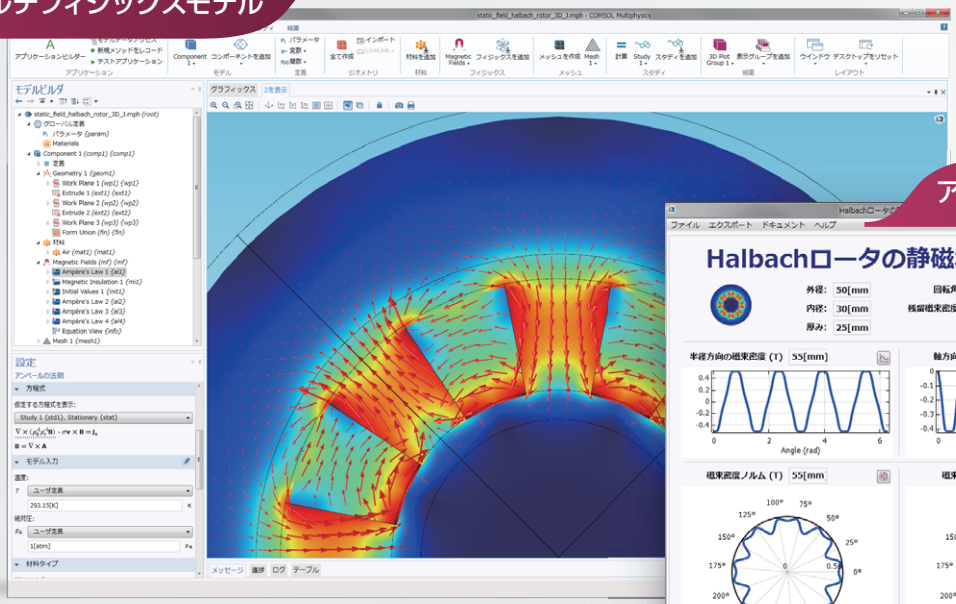

COMSOL MULTIPHYSICS®

アプリケーション

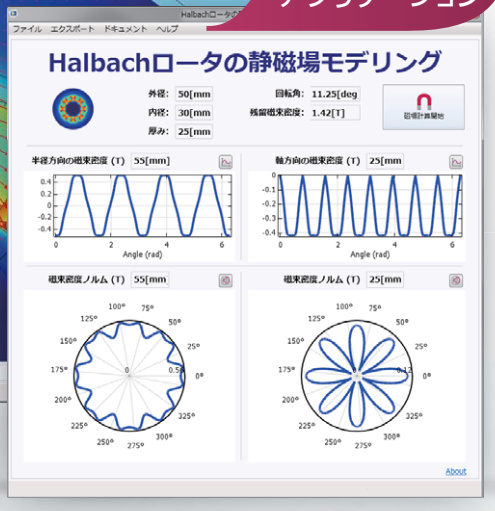

COMSOL SERVER™

～マルチフィジックスの進化論～ COMSOL Multiphysics®

Application Builder と COMSOL Server™で業務コラボレーションを実現！

Application Builder を使えば、GUI や操作性を自由にカスタマイズして、様々な目的にマッチするアプリケーションをデスクトップ上で手軽に作成できます。

アプリケーションを COMSOL Server でネットワーク共有して、次世代のコラボレーション作業が容易に実現できます。

comsol.jp/release/5.2 をご覧ください

Product Suite

- COMSOL Multiphysics®
- COMSOL Server™

電磁気・光学系
- AC/DC モジュール
- RF モジュール
- 波動光学モジュール
- 幾何光学モジュール
- MEMS モジュール
- プラズマモジュール
- 半導体モジュール

機械・構造系
- 伝熱モジュール
- 構造力学モジュール
- 非線形構造材料モジュール
- ジオメカニクスモジュール
- 疲労モジュール
- マルチボディダイナミクスモジュール
- 音響モジュール

流体系
- CFD モジュール
- ミキサーモジュール
- マイクロフルイディクスモジュール
- 地下水流モジュール
- パイプ流れモジュール
- 分子流モジュール

化学系
- 化学反応工学モジュール
- バッテリ & 燃料電池モジュール
- 電気めっきモジュール
- 腐食モジュール
- 電気化学モジュール

汎用
- 最適化モジュール
- 材料ライブラリ
- 粒子トレーシングモジュール

インタフェース
- LiveLink™ *for* MATLAB®
- LiveLink™ *for* Excel®
- CAD インポートモジュール
- デザインモジュール
- ECAD インポートモジュール
- LiveLink™ *for* SOLIDWORKS®
- LiveLink™ *for* Inventor®
- LiveLink™ *for* AutoCAD®
- LiveLink™ *for* Revit®
- LiveLink™ *for* PTC® Creo® Parametric™
- LiveLink™ *for* PTC® Pro/ENGINEER®
- LiveLink™ *for* Solid Edge®
- File Import *for* CATIA® V5

COMSOL

http://www.comsol.jp

KESCO KEISOKU ENGINEERING SYSTEM
計測エンジニアリングシステム株式会社
http://www.kesco.co.jp/comsol/
Tel : 03-5282-7040 ・ Fax : 03-5282-0808

日本磁気学会会員各位

編集委員長　早乙女英夫
論文委員長　小林宏一郎

学術講演会論文特集号発行に伴うタイトル募集について

日本磁気学会では、平成 28 年以降の学術講演会で発表した研究報告を論文として投稿し、採録された場合、学術講演会特集号論文として電子ジャーナルで発行することを理事会にて決定しました。

この特集号論文は、現在ある「Journal of the Magnetics Society of Japan」とは別に、日本語または英語での投稿を受け付ける新しい論文誌です。

そこで、学会員から新しい論文誌のタイトル（和文名と英文名）を募集します。日本磁気学会事務局あてにメール（msj@bj.wakwak.com）で応募してください。

締め切りは、1 月 22 日です。採択者には、「ジッキー」のグッズ（非売品）を贈呈します。

Journal of the Magnetics Society of Japan

Vol. 40, No. 1

Electronic Journal URL: https://www.jstage.jst.go.jp/browse/msjmag

CONTENTS

J. Magn. Soc. Jpn., **40**, 1-7 (2016) <Paper>

Design Parameter and Anisotropy Constant Ratio for Heat-Assisted Magnetic Recording

T. Kobayashi, Y. Isowaki, and Y. Fujiwara
Graduate School of Engineering, Mie Univ., *1577 Kurimamachiya-cho, Tsu 514-8507, Japan*

A design guideline for heat-assisted magnetic recording (HAMR) is presented with a view to obtaining a minimized anisotropy constant ratio K_u / K_{bulk} for media by using a model calculation. We investigated the relationship between the design parameters and the limiting factors of HAMR design. The parameters, namely the writing temperature T_w and recording layer thickness h, are related to the medium thermal stability factor of the limiting factor. In addition, inter-grain exchange coupling J is related to the statistical thermal stability factor. HAMR combined with shingled magnetic recording (SHAMR) has the advantage of reducing the medium thermal gradient, and increasing T_w is also effective in increasing the heat-transfer thermal gradient of the limiting factor. The combination of increasing h and SHAMR or increasing J and SHAMR can successfully reduce K_u / K_{bulk}. Furthermore, K_u / K_{bulk} can be reduced by the combination of increasing T_w and SHAMR.

Key words: heat-assisted magnetic recording, media design, anisotropy constant ratio, thermal stability factor, thermal gradient

1. Introduction

Heat-assisted magnetic recording (HAMR) has been proposed with the aim of solving the trilemma problem[1] of magnetic recording. HAMR is a recording method in which the medium is heated to reduce the coercivity at the time of writing.

We have already reported the design method for HAMR[2, 3]. We have introduced a new parameter, the anisotropy constant ratio K_u/K_{bulk}, which is the intrinsic ratio of film anisotropy constant K_u to bulk K_u [2]. If the K_u/K_{bulk} values for two media are identical, the difficulties involved in preparing those media are the same, even if the K_u values are different. On the other hand, increasing K_u/K_{bulk} is a challenging task. Therefore, it is necessary to design a medium with a smaller K_u/K_{bulk}. The many relationships between design parameters and K_u/K_{bulk} have been revealed[3]. We have reported the dependence of K_u/K_{bulk} on one parameter change. As a result, we find that increasing the writing temperature T_w is only effective for reducing K_u/K_{bulk} when we compare the K_u/K_{bulk} value calculated using standard parameter values. Although the combination of more than two parameters may be expected to reduce K_u/K_{bulk}, it is difficult to examine all parameter combinations. Our method is a model calculation, and it is easy to understand the physical meanings of the parameters.

In this study, we investigate the relationship between the design parameters and limiting factors of HAMR design with the aim of reducing K_u/K_{bulk}, and we provide the examination results of K_u/K_{bulk} for the combination of more than two parameters.

2. Media Design Method

From the following four conditions, we estimated whether or not the media have the potential for HAMR. That is, information stability (1) during 10 years of archiving, (2) on the trailing side located 1 bit from the writing position during writing, (3) in adjacent tracks during rewriting, and (4) under the main pole during rewriting[2, 3].

(1) The first condition, namely the information stability during 10 years of archiving, is expressed as

$$\frac{K_u(T_a)V_m}{kT_a} \geq \mathrm{TSF}_{10}, \qquad (1)$$

where $K_u(T_a)V_m/kT_a$ is a medium thermal stability factor, T_a is the ambient temperature (assumed to be 330 K), which is the maximum working temperature of the hard drive, V_m is the grain volume for the mean grain size, k is the Boltzmann constant, and TSF_{10} is the statistical thermal stability factor during 10 years of archiving.

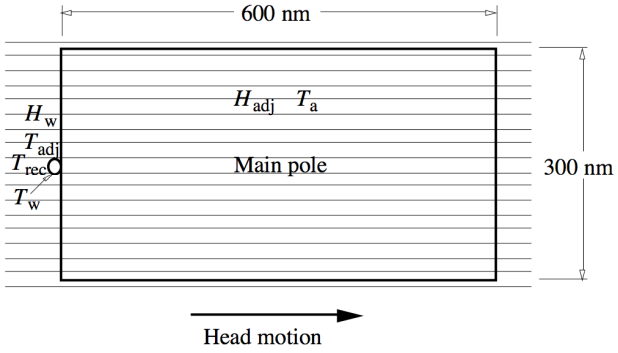

Fig. 1 Schematic illustration of writing-head configuration.

Figure 1 shows the writing-head configuration. It is assumed that the main-pole size of the head is 600 nm (down-track direction) × 300 nm (cross-track

direction), and the writing position is located on the trailing side of the main pole. The maximum temperature under the main pole is T_a.

(2) The second condition, namely the information stability on the trailing side during writing, is expressed as

$$\frac{\Delta T}{\Delta x} = \frac{T_w - T_{rec}}{\Delta x} \le \frac{\partial T}{\partial x}, \qquad (2)$$

where $\Delta T/\Delta x$ is the medium thermal gradient for the down-track direction, T_w is the writing temperature, and T_{rec} is the maximum temperature at which the information on the trailing side can be held during writing as shown in Fig. 1. Δx is the distance from the position of T_w to that of T_{rec}, and $\partial T/\partial x$ is the heat-transfer thermal gradient for the down-track direction.

(3) The third condition, namely the information stability in adjacent tracks during rewriting, is expressed as

$$\frac{\Delta T}{\Delta y} = \frac{T_w - T_{adj}}{\Delta y} \le \frac{\partial T}{\partial y}, \qquad (3)$$

where $\Delta T/\Delta y$ is the medium thermal gradient for the cross-track direction, and T_{adj} is the maximum temperature at which the information in adjacent tracks can be held during rewriting as shown in Fig. 1. Δy is the distance from the position of T_w to that of T_{adj}, and $\partial T/\partial y$ is the heat-transfer thermal gradient for the cross-track direction. $\Delta T/\Delta x$ and $\Delta T/\Delta y$ are the minimum thermal gradients required by the medium for information stability. $\partial T/\partial x$ and $\partial T/\partial y$ are the thermal gradients calculated by a heat-transfer simulation[3].

(4) The fourth condition, namely the information stability under the main pole during rewriting, is expressed as

$$H_{adj} \ge H_w, \qquad (4)$$

where H_{adj} is the maximum head field that can hold the information under the main pole, and H_w is the writing field at the position of T_w as shown in Fig. 1.

The details have been reported elsewhere[3].

The HAMR media were designed to obtain the minimum K_u/K_{bulk} value using the procedure shown in Fig. 2[3]. First, the design parameters and K_u/K_{bulk} = 1 were set. Four HAMR conditions (1), (2), (3), and (4) were examined after determining the composition of the recording layer. If there are some margins for all four conditions, K_u/K_{bulk} can be reduced. When one of the four conditions reaches the limit, the minimum K_u/K_{bulk} value can be determined. That condition becomes a limiting factor.

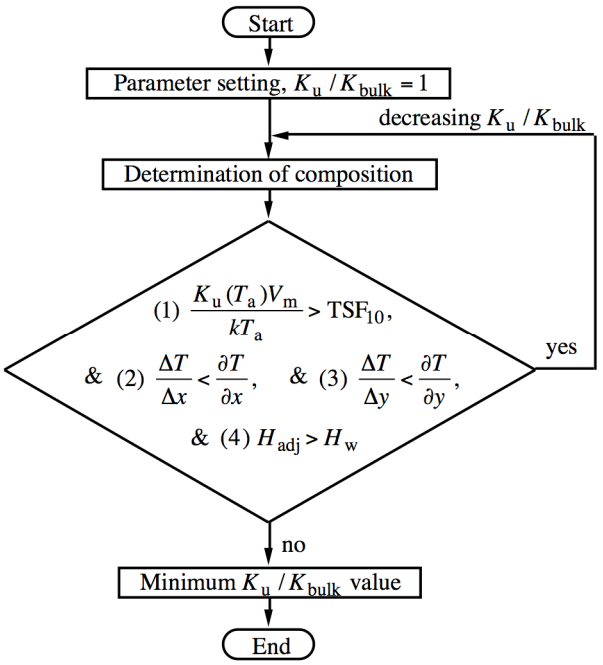

Fig. 2 HAMR media design procedure for obtaining the minimum K_u/K_{bulk} value[3].

The medium was assumed to be granular. The standard parameter values of the media design are summarized in Table 1. The bit area S is fixed, and S is the product $d_B \times d_T$ of the bit pitch d_B and the track pitch d_T. The method for determining d_T/d_B was reported in a previous paper[2]. The arrangement of the grains is not considered. The effective track width d_{ET} has been explained in a previous paper[3]. The standard medium consists of four layers, that is, a recording layer RL (Fe-Pt base, thickness h = 8 nm), interlayer 1 IL1 (MgO base, 5 nm), interlayer 2 IL2 (Cr base, 10 nm), and a heat-sink layer HSL (Cu base, 30 nm). D_m is the mean grain size, and $V_m = D_m^2 \times h$. The inter-grain exchange coupling J [4] is a newly introduced design parameter. A comparison of magnetic recording (MR) method was carried out of HAMR and HAMR combined with shingled magnetic recording (SHAMR). The light-spot diameter d_L and the heat-spot diameter d_w have also been defined in previous papers[2, 3].

Figure 3 (a) is a schematic illustration of the area near the writing position for HAMR. The writing field H_w is applied to a wide area including the writing position. The circle denoted by T_w is an isotherm of T_w, and d_w is the heat-spot diameter. The white regions indicate upward or downward magnetization, and the gray regions indicate the magnetization transition. The transition region spreads to adjacent tracks as a result of rewriting operations on the ith track.

On the other hand, the maximum rewriting number for SHAMR is considerably smaller than that for HAMR since the tracks are laid to overlap each other as shown in Fig. 3 (b).

Table 1 Standard parameter values of media design.

User areal density (Tbpsi)	4
Bit area S (nm^2)	140
Effective track width d_{ET} (nm)	10
Ambient temperature T_a (K)	330
Writing temperature T_w (K)	500
Grain number per bit n (grain / bit)	4
RL thickness h (nm)	8
Standard deviation of grain size σ_D / D_m (%)	10
Inter - grain exchange coupling J (erg / cm^2)	0
MR method	HAMR
Light - spot diameter d_L (nm)	9.0
Heat - spot diameter d_w (nm)	10
Linear velocity v (m / s)	10
Thermal conductivity of IL1 K (W / (cmK))	0.5

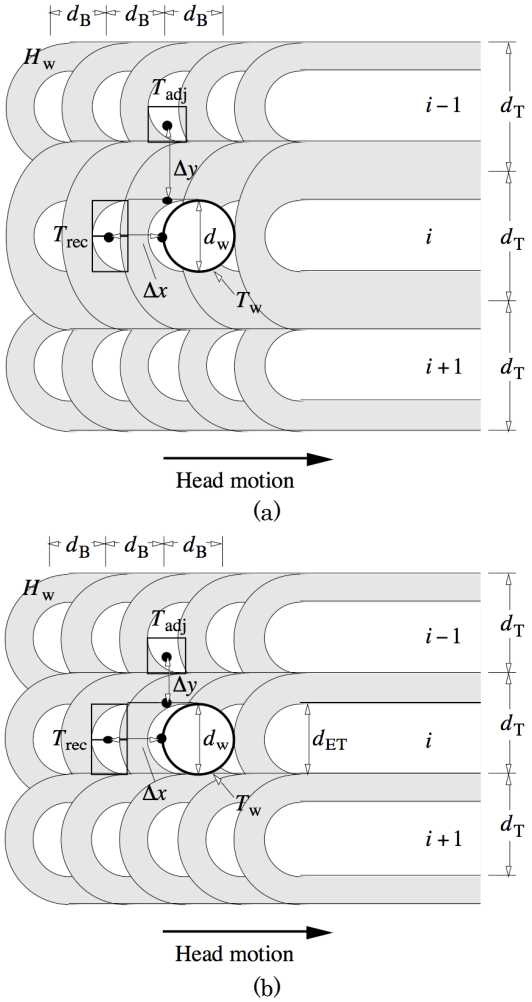

Fig. 3 Schematic illustrations of writing position for (a) HAMR and (b) SHAMR.

3. Design Parameters and Limiting Factors

We have reported the dependence of K_u / K_{bulk} on one parameter change[3]. As a result, increasing T_w is only effective for reducing K_u / K_{bulk} when we compare the K_u / K_{bulk} value calculated using standard parameter values. Increasing J from 0 to 0.19 erg/cm^2 has little effect. Although the combination of more than two parameters may be expected to reduce K_u / K_{bulk}, it is difficult to examine all parameter combinations. Therefore, we investigated the relationship between the parameters and the limiting factors. Conditions (2) and (3) can be combined as

$$\frac{\Delta T}{\Delta x} = \frac{\Delta T}{\Delta y} \le \frac{\partial T}{\partial x} = \frac{\partial T}{\partial y}, \qquad (5)$$

since $\partial T / \partial x \approx \partial T / \partial y$[2]. Condition (4) has some margins for all the cases we examined. Therefore, the major limiting factors in the media design are condition (I) given by Eq. (1) ($K_u(T_a)V_m / kT_a \ge \mathrm{TSF}_{10}$) and condition (II) given by Eq. (5) (hereafter, shown as $\Delta T / \Delta x = \Delta T / \Delta y \equiv \Delta T / \Delta x(y)$, $\partial T / \partial x = \partial T / \partial y \equiv \partial T / \partial x(y)$, and $\Delta T / \Delta x(y) \le \partial T / \partial x(y)$).

3.1 Condition (I) - increasing $K_u(T_a)V_m / kT_a$

$K_u(T_a)V_m / kT_a$ must be increased or TSF_{10} decreased to relax condition (I) given by Eq. (1) $K_u(T_a)V_m / kT_a \ge \mathrm{TSF}_{10}$. First, we discuss the parameter for increasing $K_u(T_a)$.

Figure 4 (a) shows the dependence of $K_u(300\ \mathrm{K})$ on Curie temperature T_c, in which the calculation parameter is K_u / K_{bulk}. The dotted line shows the $K_u(300\ \mathrm{K})$ value that satisfies $K_u(T_a)V_m / kT_a = \mathrm{TSF}_{10}$. Although the $K_u(T_a)$ value that satisfies $K_u(T_a)V_m / kT_a = \mathrm{TSF}_{10}$ is independent of T_c, the $K_u(300\ \mathrm{K})$ value that satisfies $K_u(T_a)V_m / kT_a = \mathrm{TSF}_{10}$ increases as T_c decreases, and it diverges at T_a = 330 K. The intersections of the solid lines and the dotted line show the K_u / K_{bulk} dependence that satisfies $K_u(T_a)V_m / kT_a = \mathrm{TSF}_{10}$ on T_c. Therefore, the required K_u / K_{bulk} can be reduced by increasing T_c, and then, K_u / K_{bulk} can be reduced by increasing T_w as shown in Fig. 4 (b). In other words, if K_u / K_{bulk} is constant, increasing T_w is effective for increasing $K_u(T_a)$. If T_w is low, the extra K_u / K_{bulk} is needed to realize HAMR.

Furthermore, K_u / K_{bulk} is a function of the heat-transfer thermal gradient $\partial T / \partial x(y)$ as shown in Fig. 4 (c). As $\partial T / \partial x(y)$ increases, K_u / K_{bulk} first becomes lower, and then becomes constant with respect to $\partial T / \partial x(y)$. In the range where K_u / K_{bulk} changes, the limiting factor is condition (II) $\Delta T / \Delta x(y) \le \partial T / \partial x(y)$. And it is condition (I) $K_u(T_a)V_m / kT_a \ge \mathrm{TSF}_{10}$ in the range where K_u / K_{bulk} is constant. The constant K_u / K_{bulk} value in Fig. 4 (c) corresponds to that in Fig. 4 (b). Although increasing T_w is effective for reducing K_u / K_{bulk} (Fig. 4 (b)), a higher $\partial T / \partial x(y)$ is needed to obtain a lower K_u / K_{bulk} (Fig. 4 (c)). The closed circles show the K_u / K_{bulk} values and their $\partial T / \partial x(y)$ values calculated for the standard medium structure and the standard thermal constants[2]. Increasing T_w is effective for reducing K_u / K_{bulk} in consideration of calculated $\partial T / \partial x(y)$.

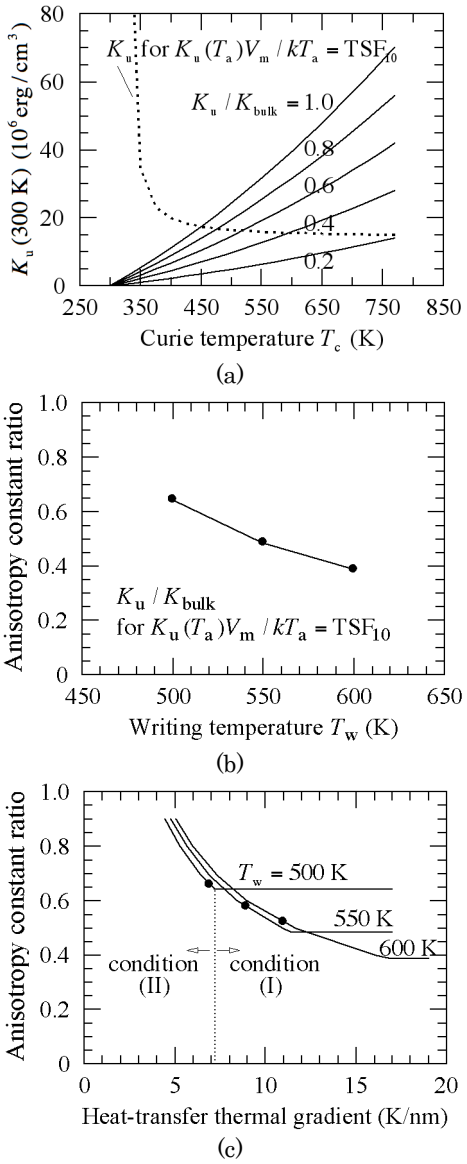

Fig. 4 (a) Dependence of anisotropy constant $K_u(300\text{ K})$ on Curie temperature T_c, (b) dependence of anisotropy constant ratio K_u/K_{bulk} on writing temperature T_w, and (c) dependence of K_u/K_{bulk} on heat-transfer thermal gradient $\partial T/\partial x(y)$.

Next, we discuss the parameter for increasing V_m.

One way of increasing $V_m = D_m^2 \times h$ is to reduce the grain number per bit n. Although TSF$_{10}$ becomes larger as n becomes smaller[4], $D_m = \sqrt{S/n} - \Delta$ increases as n decreases where S is the bit area and Δ = 1 nm is the non-magnetic spacing between grains (*e.g.*, D_m = 4.92 nm for n = 4). The solid line, in the range where K_u/K_{bulk} is constant in Fig. 5, becomes noticeably low as n decreases. In that range, the limiting factor is condition (I) as mentioned above. Therefore, reducing n relaxes condition (I) through increasing V_m. Furthermore, the closed circles can also be reduced as n decreases. Therefore, reducing n is effective for reducing K_u/K_{bulk}. When we compare (a) T_w = 500 K and (b) 550 K, the n dependence of the K_u/K_{bulk} values of the closed circles is reduced by increasing T_w since the limiting factor becomes condition (II).

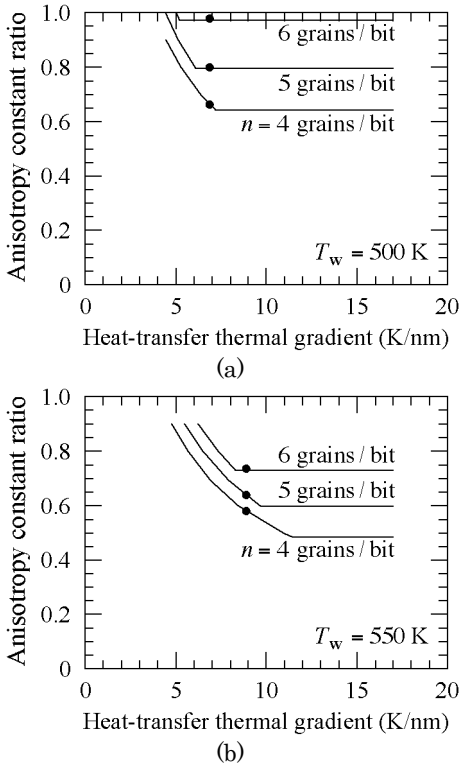

Fig. 5 Dependence of K_u/K_{bulk} on $\partial T/\partial x(y)$ at (a) T_w = 500 K and (b) 550 K (calculation parameter: grain number per bit n).

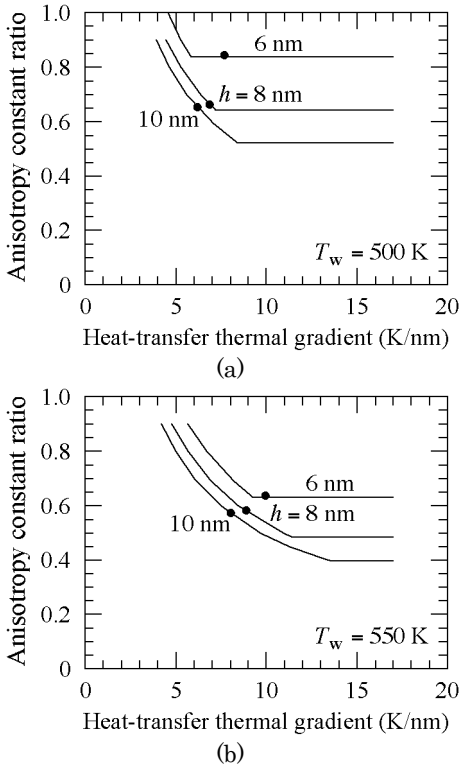

Fig. 6 Dependence of K_u/K_{bulk} on $\partial T/\partial x(y)$ at (a) T_w = 500 K and (b) 550 K (calculation parameter: RL thickness h).

Another way of increasing $V_m = D_m^2 \times h$ is to increase the RL thickness h. It can also be seen from the solid lines where K_u / K_{bulk} is constant in Fig. 6 that increasing h relaxes condition (I). However, when h increases from the standard value of 8 to 10 nm, the K_u / K_{bulk} values of the closed circles are almost the same for both (a) T_w = 500 K and (b) 550 K since the limiting factor is condition (II), and $\partial T / \partial x(y)$ is decreased by increasing h due to the adiabatic effect of RL[2]. If $\Delta T / \Delta x(y)$ can be decreased or $\partial T / \partial x(y)$ can be increased in some way, increasing h will be effective for reducing K_u / K_{bulk}. The way of decreasing $\Delta T / \Delta x(y)$ will be discussed in **3.3**, and the combination of the parameters will be discussed in **3.5**.

3.2 Condition (I) - decreasing TSF_{10}

TSF_{10} must be decreased to relax condition (I) given by Eq. (1) $K_u(T_a)V_m / kT_a \geq TSF_{10}$.

One way of decreasing TSF_{10} is to reduce the standard deviation of the grain size σ_D / D_m [4]. Decreasing σ_D / D_m relaxes condition (I) as seen from the solid lines in Fig. 7. Furthermore, the K_u / K_{bulk} values of the closed circles can be reduced by decreasing σ_D / D_m as shown in Fig. 7 (a). However, it seems that σ_D / D_m cannot be reduced from the standard value of 10 %.

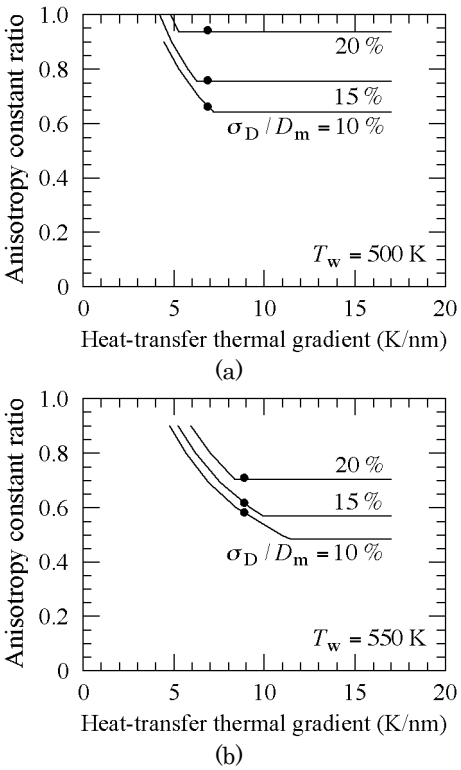

Fig. 7 Dependence of K_u / K_{bulk} on $\partial T / \partial x(y)$ at (a) T_w = 500 K and (b) 550 K (calculation parameter: standard deviation of grain size σ_D / D_m).

In Fig. 7 (b), it should be noted that the difference between the K_u / K_{bulk} values of the closed circles (σ_D / D_m = 10 % and 15 %) is very small. If T_w can be increased, a relatively large σ_D / D_m value may be allowable.

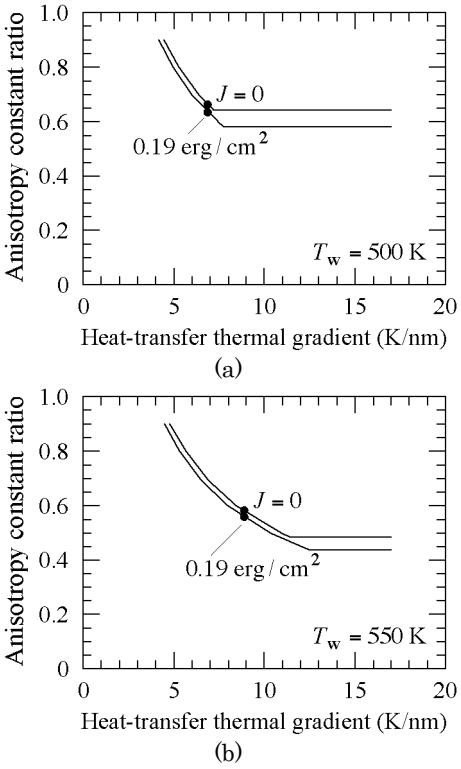

Fig. 8 Dependence of K_u / K_{bulk} on $\partial T / \partial x(y)$ at (a) T_w = 500 K and (b) 550 K (calculation parameter: inter-grain exchange coupling J).

Although another way of decreasing TSF_{10} is to introduce inter-grain exchange coupling J [4] as seen from the solid lines in Fig. 8. J = 0.19 erg/cm^2 corresponds to an inter-grain exchange coupling e_m of 1.1[4] for D_m. The inter-grain exchange coupling e makes the statistical thermal stability factor e times larger. It has little effect on reducing the K_u / K_{bulk} values of the closed circles since the limiting factor is condition (II). As seen from Fig. 8 (b), increasing T_w has little effect for the same reason. If $\Delta T / \Delta x(y)$ can be decreased or $\partial T / \partial x(y)$ can be increased in some way, introducing J will also be effective for reducing K_u / K_{bulk}. The combination of the parameters will be discussed in **3.5**.

3.3 Condition (II) - decreasing $\Delta T / \Delta x(y)$

$\Delta T / \Delta x(y)$ must be decreased or $\partial T / \partial x(y)$ increased to relax condition (II) given by Eq. (5) $\Delta T / \Delta x(y) \leq \partial T / \partial x(y)$.

Introducing SHAMR is effective for decreasing $\Delta T / \Delta x(y)$ as seen from the solid lines where K_u / K_{bulk} changes in Fig. 9 (a). T_{adj} in Eq. (3) for SHAMR is higher than that for HAMR since the maximum rewriting number for SHAMR is considerably smaller than that for HAMR[3]. However, the K_u / K_{bulk} values of the closed circles are almost the same since the limiting factor is condition (I). If we

can find a way to increase $K_u(T_a)V_m/kT_a$ or decrease TSF_{10}, introducing SHAMR will be effective for reducing K_u/K_{bulk}. Figure 9 (b) shows the results for T_w = 550 K. Since the limiting factor can be changed to condition (II), introducing SHAMR becomes effective.

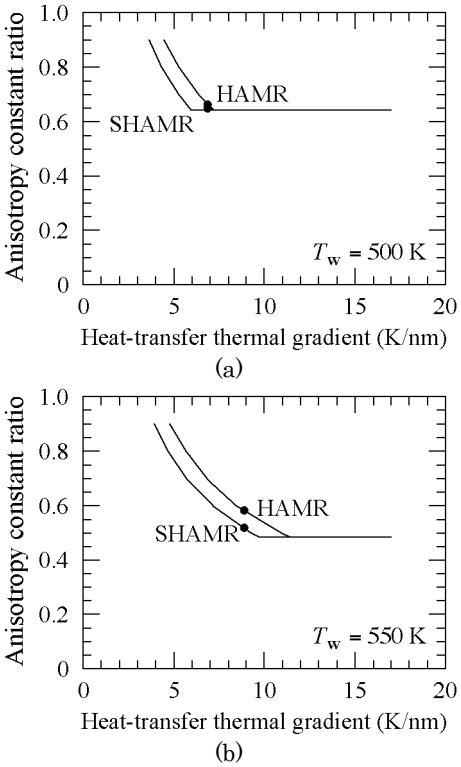

Fig. 9 Dependence of K_u/K_{bulk} on $\partial T/\partial x(y)$ at (a) T_w = 500 K and (b) 550 K (calculation parameter: HAMR and SHAMR).

3.4 Condition (II) - increasing $\partial T/\partial x(y)$

Although increasing T_w is effective for increasing $\partial T/\partial x(y)$ as mentioned above in **3.1**, $\partial T/\partial x(y)$ can be changed very little by changing the parameters, namely the light-spot diameter d_L, the heat-spot diameter d_w, and the linear velocity v [3]. If the thermal conductivity K of IL1 decreases from 0.5 W/(cmK), $\partial T/\partial x(y)$ becomes smaller as shown in a previous paper[3]. One possibility for increasing $\partial T/\partial x(y)$ involves examining a media structure with a large $\partial T/\partial x(y)$.

3.5 Combination of parameters

The combination of one parameter that relaxes condition (I) and another that relaxes condition (II) may be useful for reducing K_u/K_{bulk}.

When we replaced parameter h = 8 nm with 10 nm, K_u/K_{bulk} changed from 0.66 to 0.65, and when only SHAMR was utilized, K_u/K_{bulk} became 0.64 at T_w = 500 K. Alone they had scarcely any effect on reducing K_u/K_{bulk}. Next, we combined h = 10 nm, which increases $K_u(T_a)V_m/kT_a$ of condition (I), and SHAMR, which decreases $\Delta T/\Delta x(y)$ of condition (II). Figure 10 (a) shows the result of the combination, and the resultant K_u/K_{bulk} is 0.58. The case where T_w = 550 K is shown in Fig. 10 (b). When we compare HAMR and SHAMR, we find that SHAMR is more effective. This can be explained by Fig. 9 (b). On the other hand, when we compare a SHAMR of h = 8 nm and a SHAMR of h = 10 nm, the K_u/K_{bulk} values are almost the same since the limiting factor is condition (II) as seen in Fig. 6.

Therefore, the design parameters of HAMR, SHAMR, h, and T_w are related in a complex manner in terms of reducing K_u/K_{bulk}.

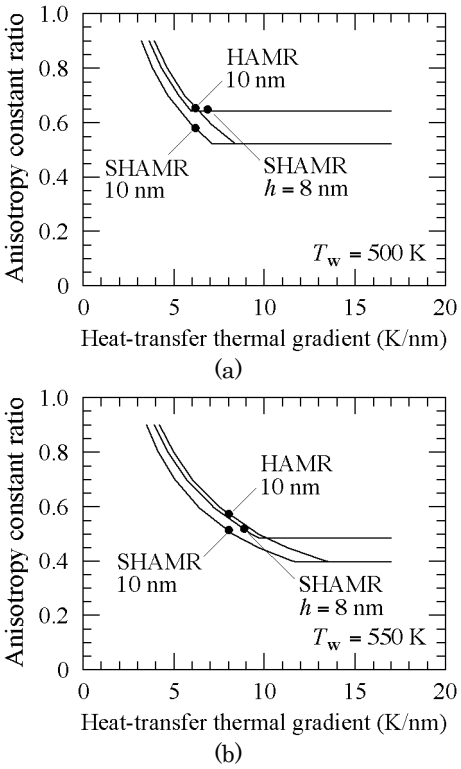

Fig. 10 Dependence of K_u/K_{bulk} on $\partial T/\partial x(y)$ at (a) T_w = 500 K and (b) 550 K (calculation parameter: HAMR, SHAMR, and h).

Next, we consider the relationship between HAMR, SHAMR, J, and T_w.

We combined J = 0.19 erg/cm², which decreases TSF_{10} of condition (I), and SHAMR, which decreases $\Delta T/\Delta x(y)$ of condition (II). Figure 11 (a) shows the result of the combination, and the resultant K_u/K_{bulk} is 0.58. The case of T_w = 550 K is shown in Fig. 11 (b). When we compare a SHAMR of J = 0 and a SHAMR of J = 0.19 erg/cm², the K_u/K_{bulk} values are almost the same since the limiting factor is condition (II).

The results are summarized in Fig. 12. The standard K_u/K_{bulk} value (calculated using the standard parameter values) is 0.66. The parameters T_w, h, and J relax condition (I) $K_u(T_a)V_m/kT_a \geq TSF_{10}$, and the K_u/K_{bulk} values become 0.58, 0.65, and 0.63, respectively, by changing the parameters. And the parameters HAMR or SHAMR and T_w relax condition (II) $\Delta T/\Delta x(y) \leq \partial T/\partial x(y)$, and the K_u/K_{bulk}

values become to be 0.64 and 0.58, respectively.

If h = 10 nm and SHAMR or J = 0.19 erg/cm^2 and SHAMR are combined, K_u/K_{bulk} = 0.58 can be achieved without increasing T_w. A lower T_w is better from the viewpoint of the heat resistance of the writing head and/or the surface lubricant.

If T_w can be increased to 550 K, we can expect a K_u/K_{bulk} value of 0.51 by combination with SHAMR.

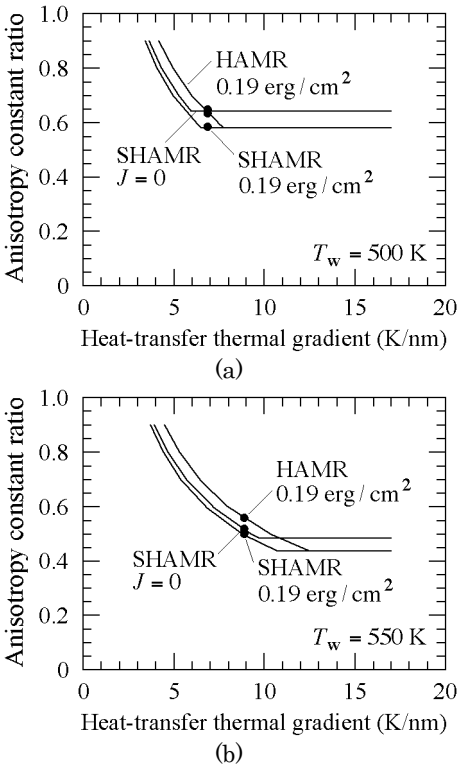

Fig. 11 Dependence of K_u/K_{bulk} on $\partial T/\partial x(y)$ at (a) T_w = 500 K and (b) 550 K (calculation parameter: HAMR, SHAMR, and J).

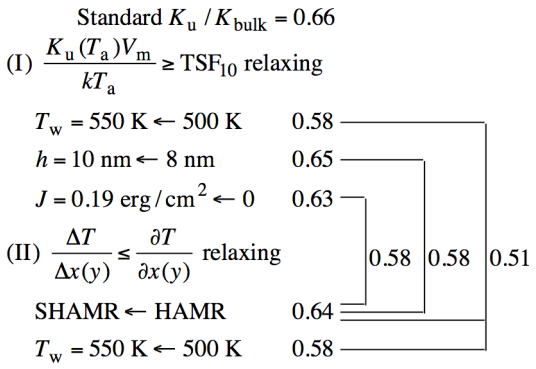

Fig. 12 Media design guideline.

4. Conclusions

The major limiting factors as regards obtaining the minimum anisotropy constant ratio K_u/K_{bulk} for media are (I) the information stability during 10 years of archiving and (II) the information stability on the trailing side during writing and in adjacent tracks during rewriting.

The parameters, namely the writing temperature T_w, the recording layer thickness h, and the inter-grain exchange coupling J, relax condition (I). On the other hand, HAMR combined with shingled magnetic recording (SHAMR) and T_w relax condition (II).

The combination of one parameter that relaxes condition (I) and another that relaxes condition (II) is useful for reducing K_u/K_{bulk}. If increasing h and SHAMR or increasing J and SHAMR are combined, K_u/K_{bulk} can be reduced successfully without increasing T_w. If T_w can be increased, K_u/K_{bulk} will be reduced by the combination with SHAMR.

It is important for the media design to distinguish whether the limiting factor is condition (I) or (II).

Acknowledgements We acknowledge the support of the Storage Research Consortium (SRC), Japan.

References

1) S. H. Charap, P.-L. Lu, and Y. He: *IEEE Trans. Magn.*, **33**, 978 (1997).
2) T. Kobayashi, Y. Isowaki, and Y. Fujiwara: *J. Magn. Soc. Jpn.*, **39**, 8 (2015).
3) T. Kobayashi, Y. Isowaki, and Y. Fujiwara: *J. Magn. Soc. Jpn.*, **39**, 139 (2015).
4) Y. Isowaki, T. Kobayashi, and Y. Fujiwara: *J. Magn. Soc. Jpn.*, **38**, 1 (2014).

Received Apr. 12, 2015; Revised Jun. 17, 2015; Accepted Oct. 8, 2015

J. Magn. Soc. Jpn., **40**, 8-12 (2016) <Paper>

The hysteresis properties analysis of Fe-4 wt% Si prepared by high purity metallurgy

Z. Lei, T. Horiuchi, I. Sasaki, C. Kaido*, M. Takezawa**, S. Hata***, Y. Horibe**, T. Ogawa****, H. Era**
Kyushu Institute of Technology, *2-4 Hibikino, Wakamatsu-ku, Kitakyushu-shi, Fukuoka, 808-0196, Japan*
*National Institute of Technology, Kitakyushu College, *5-20-1 Shii, Kokuraminami-ku, Kitakyushu-shi, Fukuoka, 802-0985, Japan*
**Kyushu Institute of Technology, *1-1 Sensui-cho, Tobata-ku, Kitakyushu-shi, Fukuoka, 804-0015, Japan*
***Kyushu University, *6-1 Kasugakoen, Kasuga, Fukuoka, 816-8580, Japan*
****Mechanics & Electronics Research Institute, Fukuoka Industrial Technology Center, *3-6-1, Norimatsu, Yahatanishi-ku, Kitakyushu-shi, 807-0831, Japan*

An investigation on the improvement in hysteresis properties of high purity Fe-4 wt% Si prepared by cold crucible levitation melting was presented compared with a Fe-0.1 wt% C- 4 wt% Si alloy formed by the identical process. The results showed that thin elongated carbon compounds were precipitated in both grains and grain boundaries of Fe-0.1 wt% C- 4 wt% Si sample observed by means of Kerr effect microscopy and STEM, leading to an apparent degradation in coercivity, permeability and hysteresis loss. With regard to hysteresis loss in Fe-4 wt% Si, it increases linearly with the increase of maximum magnetic flux density below 1.4 T, whereas for Fe-0.1 wt% C- 4 wt% Si, it behaves nonlinearly even at low maximum magnetic flux density and rises sharply with the increase of maximum magnetic flux density. Additionally, the precipitated carbon compounds in the grain boundaries change the morphology of the grain boundaries.

Key words: Fe-4 wt% Si, high purity, hysteresis loss, magnetic domain

1. Introduction

The iron loss P_{loss} of electrical steel can be divided into three components: hysteresis loss P_h, classical eddy current loss P_e, and anomalous loss P_a according to the equation:

$$P_{loss} = P_h + P_e + P_a \quad (1)$$

Among the three components, hysteresis loss is the fundamental loss in electrical steel, especially at high magnetic flux density in the typical frequency range of transformers. Hysteresis loss is typically associated with obstacles to domain wall motion such as grain boundaries, precipitates [1] and crystallographic orientations [2]. The improvement possibility in hysteresis loss of silicon iron alloy by reducing impurities has been recognized clearly [3, 4]. Kaido et al. [1] gave a theoretical calculation about the effect of the precipitates on the hysteresis loss by reducing impurities further than commercial non-oriented steel 35H210, and their results turned out that the influence can be decreased substantially to 1/4. On the other hand, the eddy-current loss is closely related to the domain size and mobility of domain wall [5], which also can be significantly influenced by the existence of precipitates, and its mechanism has been reported by several authors [6-8].

Most of the precipitates are originated from exterior impurities during a series of metallurgy processes and reduction of impurities is running up against potency in the conventional metallurgy processes. Therefore, in this current study, a method called cold crucible levitation melting (CCLM) was embraced to minimize the impurities in the ingots. The most important feature of CCLM is that the molten alloy can be levitated from the cold crucible by magnetic force, so as to reduce the impurities apparently by isolating the contamination from the crucible during melting [9]. Meanwhile, highly pure raw iron and silicon with a purity of 99.99 wt% and 99.999 wt% respectively were utilized to prepare the alloys.

In this paper, to clarify the potential of improvement in hysteresis properties by high purity, Fe-4 wt% Si alloy was firstly prepared by CCLM. Another Fe-4 wt% Si alloy with 0.1 wt% carbon added was also prepared as a comparison to reveal the effect of carbon on the magnetic properties and its interaction with domain structures. The permeability, coercivity and hysteresis loss of both alloys were studied. Additionally, the morphology of microstructure and the demagnetized domain structure were investigated by means of Kerr effect microscopy. The factors which influenced the hysteresis properties were discussed in detail by taking the domain structure and microstructure into consideration.

2. Materials and methods

Two kinds of Fe-4 wt% Si samples without and with addition of 0.1 wt% carbon were used for this study, identified as 4N and 3N. Two samples were both prepared from raw iron and silicon with a purity of 99.99 wt% and 99.999 wt% respectively in CCLM under high vacuum, except 3N with addition of 0.1 wt% carbon (99.999 wt%), which can be summarized as 4N (Fe-4 wt% Si) and 3N (Fe-0.1 wt% C-4 wt% Si). The detail of the identical CCLM furnace and its effect of impurities elimination, the homogeneity of element distribution can be found in the papers [10, 11]. Both the

samples were maintained at melted condition and stirred for about 20 min at approximately 1600 °C, then followed by furnace cooling to room temperature (without subsequent annealing).

Hysteresis loops were measured at maximum magnetization from approximately 0.5 T to 1.5 T, and 5000 A/m applied field on both 5-mm-thick ring samples of 35 mm inner and 45 mm external diameter. These tests were performed under direct current (DC) using a magnetization measurement instrument, and various hysteresis properties were calculated based on the hysteresis loops.

The samples for domain observation were cut from the ring samples. The thickness of both samples was 2.5 mm and they were both finely grounded with an adequate finish polish with 0.02 μm colloidal silica, so as to reduce the agitation of surface stress. The demagnetized domain structures were observed using Kerr effect microscopy. The determination of crystallographic direction and microstructure were performed by Electron Back-Scattered Diffraction (EBSD) equipped in a SU-70 Scanning Electron Microscopy and analyzed by Orientation Image Microscopy (OIM) software. The morphology of precipitates in 3N sample were observed by Scanning Transmission Electron Microscopy (STEM) equipped in the FEI TECNAI-F20 TEM, and its samples were prepared by ion milling after a mechanical polish to about 30 μm.

3. Results and Discussion

3.1. Hysteresis loop

The hysteresis loops in Fig. 1 show that 4N sample has better hysteresis properties with lower coercivity of 18 A/m compared with 76 A/m, and remanence of 0.32 T compared with 0.48 T of 3N. All of the compared data are summarized in Table 1. Additionally, 4N can be magnetized up to its

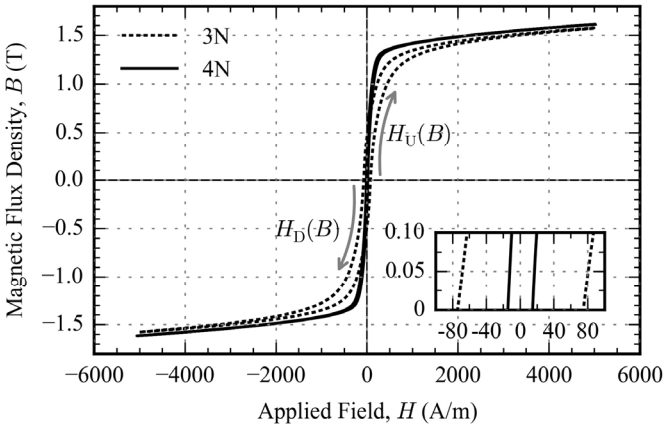

Fig. 1 DC hysteresis loops measured in 3N and 4N ring samples at maximum applied field H_m of 5000 A/m, associated with an inset for clarity of the coercivity and low magnetization part of hysteresis loops. Two arrows indicate the ascending branch $H_U(B)$ and descending branch $H_D(B)$ of hysteresis loops, respectively.

Table 1 Comparison of maximum magnetic flux density, coercivity, remanence and permeability of two samples at H_m = 5000 A/m

Hysteresis properties	4N	3N
Maximum magnetic flux density (T)	1.60	1.58
Remanence (T)	0.32	0.48
Coercivity (A/m)	18	76
Maximum permeability (H/m)	0.010	0.004
Relative maximum permeability	8000	3200

maximum permeability with value of 0.010 H/m at lower applied field of 30 A/m with comparison to 0.004 H/m of 3N at 120 A/m, which can be concluded that 4N sample can be easily magnetized to higher magnetization at lower applied field compared to 3N.

The hysteresis losses P_h in Fig. 2 are calculated from a series of hysteresis loops measured at maximum magnetic flux density B_m from approximately 0.5 T to 1.45 T, and its relationship with each corresponding B_m are shown in Fig. 2. It can be found that P_h of 4N is significantly lower than that of 3N in the whole range of B_m, especially at higher Bm. Additionally, the increase of P_h in 4N has a linear connection with B_m within the range of 0.5 and 1.45 T applied in the experiment, whereas P_h of 3N increases gradually at the low applied field and fast along with the increase of B_m.

During magnetization, it is generally agreed that 180° domain wall displacement takes place at low applied field which are mainly controlled by the second phases and grain size [12], and 90° domain wall displacement needs a fairly large magnetic field which are mainly controlled by the crystallographic texture [12]. The increment of hysteresis loss of high purity 4N sample only linearly relates with B_m, which is totally independent with the sample parameters such as grain size, texture, regardless of whether on the condition of 180° or 90° domain wall displacement stage. However, the

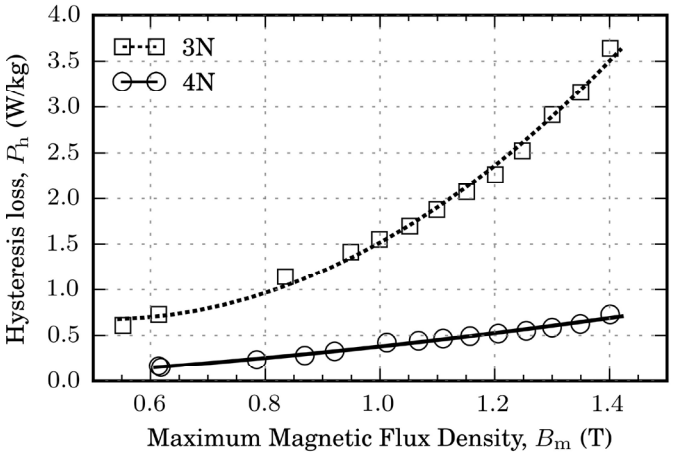

Fig. 2 Comparison of relationship of maximum flux density B_m (less than 1.45 T) and hysteresis loss P_h in 3N and 4N samples.

increment of hysteresis loss in 3N samples reveals its significant sensitivity on the structural parameters. During the 180° domain wall displacement stage at B_m lower than 0.6 T, the increment of hysteresis loss is linear without relying much on the structural variation, but at the 90° domain wall displacement stage, the energy loss dissipated by the motion of domain wall increases aggressively.

As known, hysteresis loss for ferromagnetic material is equivalent to the area of hysteresis loop, that is, $P_h = \oint HdB$. The integration can also be treated as the summation of slices of width of hysteresis loop mathematically. Each individual width $H_{CB}(B)$ of hysteresis loop can be defined as the difference of the ascending branch $H_U(B)$ and the descending branch $H_D(B)$ (see Fig. 1) at a specific magnetization B according to Eq. 3 [1]:

$$H_{CB}(B) = H_U(B) - H_D(B) \quad (3)$$

The variation of calculated $H_{CB}(B)$ as a function of B in the hysteresis loops of the two samples are shown in Fig. 3. It can be seen that $H_{CB}(B)$ maintains constantly till magnetization up to 1.2 T, then slightly increases and start to decrease afterwards in 4N sample, which is in accordance with the results of Fig. 2. As a comparison, $H_{CB}(B)$ of 3N approximately maintains as a small constant below magnetization of 0.6 T, then starts to grow gradually and finally increases abruptly to a very large value and start to decrease afterwards. This difference of hysteresis loop width during magnetization between those two samples will be discussed in the following sections by combining with the morphology of precipitates, crystallographic texture, grain and domain structure.

3.2. Effect of microstructure and phase

The phase, grain morphology and orientations of part of the two rings samples are observed by EBSD and some of the results are shown in Fig. 4. By summarizing all the results, the structure of near equiaxed grains exist in both of the samples and their average sizes are similar, which are approximately 5 mm, and the orientations of grains are random without any preferred orientations found (Fig. 4 (a) and (c)). Therefore, the influence of grain size below 0.6 T (180° domain wall displacement stage), and the influence of crystallographic orientations on the difference of hysteresis loop width above 0.6 T (90° domain wall displacement stage) in Fig. 3 can be ignored. So the big differences on hysteresis properties between the two samples are roughly considered as a consequence of the existence of precipitates introduced in by carbon concentration. The morphology of the grains in 4N (Fig. 4 (b)) is irregular polyhedron by the equilibrium growth of adjacent grains, whereas near-polyhedron in 3N (Fig. 4 (d)) with the addition influence of the carbon precipitates. On the other hand, only A2 base phases exist in

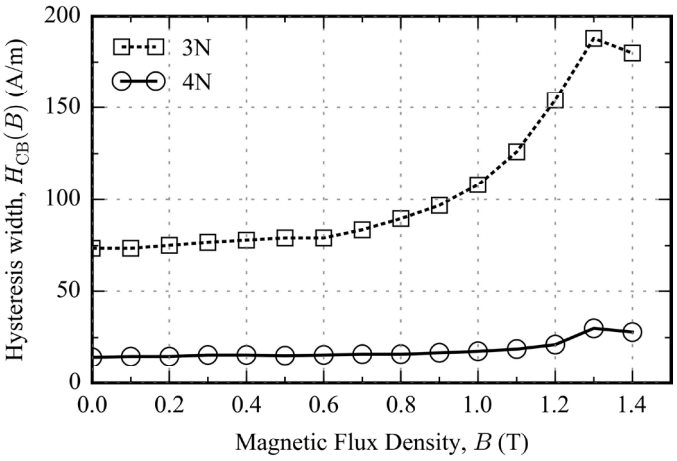

Fig. 3 Relationship of width $H_{CB}(B)$ of hysteresis loop at series of magnetic flux density B in 3N and 4N samples.

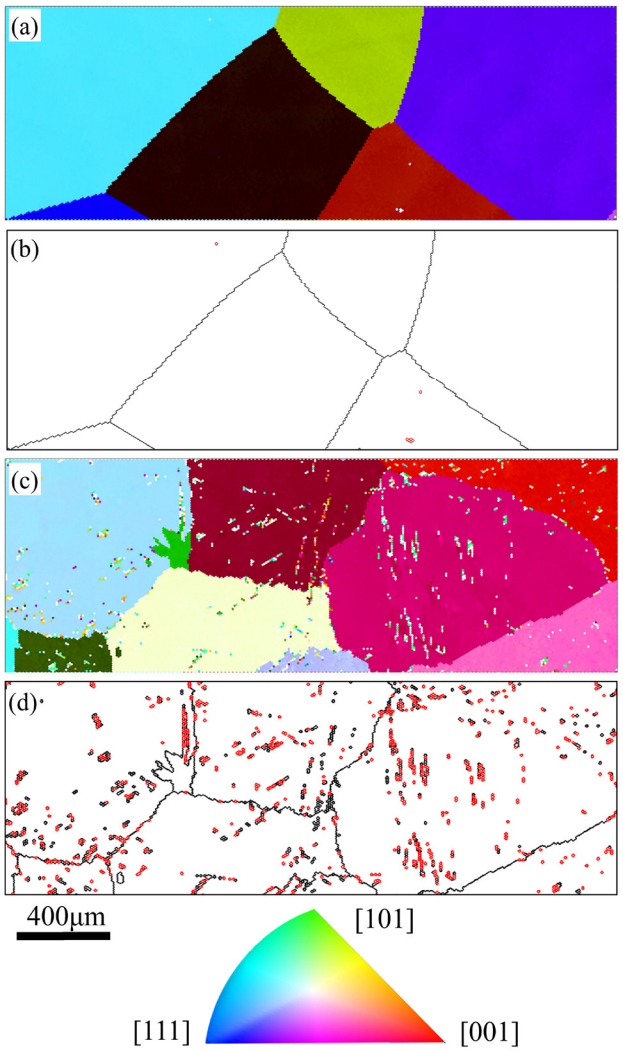

Fig. 4 Orientation maps of (a) 4N and (c) 3N samples, grain boundary maps and phase maps of (b) 4N and (d) 3N samples observed by means of EBSD. In (b) and (d). The areas surrounded by black lines represent base phases, and the areas surrounded by red lines represent the second phases.

4N (Fig. 4 (b)) but many of the second phases are precipitated in 3N indicated by the area surrounded by red lines in Fig. 4 (d). These phases are distributed in both grain and grain boundaries. Therefore, it can be stated here that the second phase is the main reason for the difference of hysteresis properties of the two samples, as well as the morphology difference of grain boundaries.

The specific morphology of the precipitates were investigated by STEM and its results are shown in Fig. 5. The overall view in Fig. 5 (a) indicates that the precipitates exist at a state of thin elongated columnar structures and aligned with each other in parallel. More specific observation in Fig. 5 (b) indicates that these precipitates grow in the grain as insertions, with a similar width of approximately 50 nm. The EDS results (center of Fig. 5) show that the carbon atoms are enriched in the precipitates, which can be considered as carbon compounds. These compounds can act as strong pinning obstacles against the structures and motion of domain wall, as demonstrated in the following section.

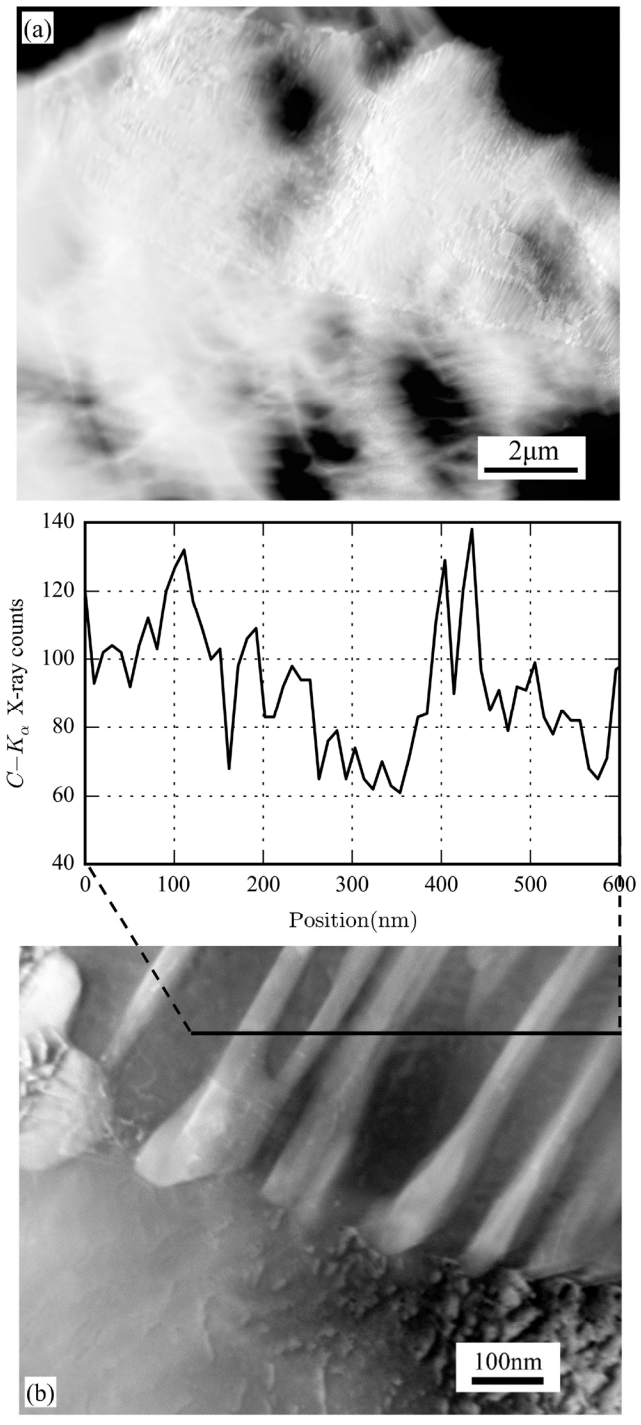

Fig. 5 The precipitates observed in the 3N by STEM high-angle annular dark-field (HAADF). (a) Observation in a wider area indicates high density of thin elongated phase, and (b) one more specific observed area in (a). The middle figure shows the EDS mapping of carbon element along the line in (b).

3.2. Domain structure

The hysteresis loss is the energy dissipated in the domain wall motion, therefore, it is important to clarify the condition of domain structures in both of the samples. Fig. 6 gives the demagnetized surface domain structures in part of each sample, from which it can be found that small complex lancet domain patterns dominates in the observed areas, and size of both surface domains are in the same order of magnitude.

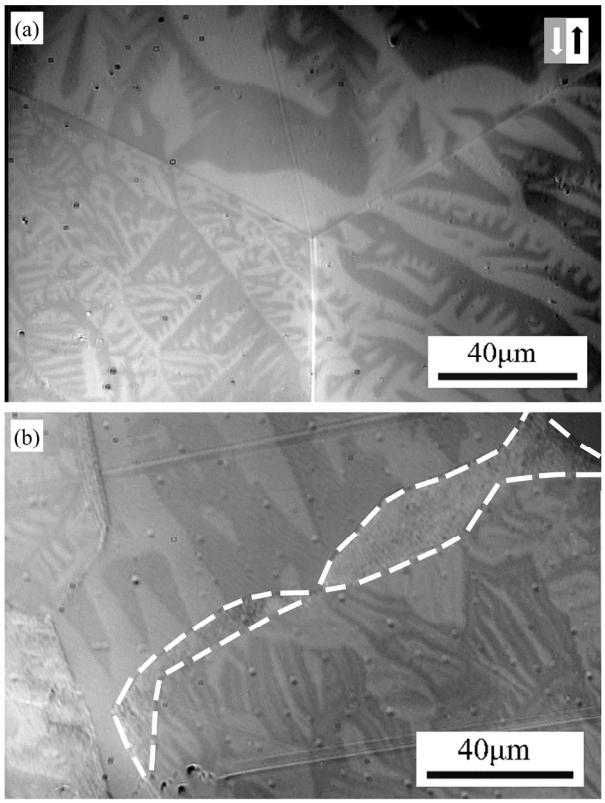

Fig. 6 The demagnetized domain structures of (a) 4N and (b) 3N samples observed by means of Kerr microscopy. The dark and bright areas indicate upward and downward magnetization components, respectively. The area surrounded by white dash lines in (b) indicate the carbon precipitates.

This proves that the precipitates dominate the difference in the hysteresis loss of the two samples, regardless of the influence of surfaces. The precipitates exist as non-magnet because no domain structures are observed in them (indicated by the arrows in Fig. 6). These non-magnetic precipitates weaken the interaction between magnetic components in the samples, resulting in the degradation of the magnetization process, which leads to the increase of hysteresis loss and reduction of permeability, which has been described previously.

It can be also found that domain structures in each individual grain of each sample differ. This kind of differences are mainly dominated by the deviation angle of the closest easy magnetization axis {001} from the sample surface, which has been reported in detail by Williams et al [5].

4. Conclusions

The hysteresis properties, specifically the relationship between hysteresis loss and maximum magnetic flux density, and magnetic domain of high purity Fe- 4 wt% Si (4N) alloy with comparison to Fe- 0.1 wt% - 4 wt% Si (3N) carbon created by CCLM were investigated.

1. High purity 4N alloy has super low coercivity, permeability and hysteresis loss than 3N, due to pinning of domain 180° and 90° wall displacement by the elongated thin carbon compounds which are distributed in both of grains and grain boundaries.
2. By increasing the purity of Fe-4 wt% Si, the relationship between hysteresis loss and maximum flux density are correlated linearly, by comparison to the nonlinear relationship in 3N.
3. The presence of carbon compounds precipitated in the grain boundaries changes the morphology of the grain boundaries. The compounds also retard the continuity of the domain structures, thus finally resulting in degradation of the hysteresis properties.

Acknowledgements This work were supported in part by the Nanotechnology Support Project of the Ministry of Education, Culture, Sports, Science, and Technology (MEXT). We also thank the support of Division of Instrumental Analysis Natural Science Center for Research and Education, Kagoshima University, Japan, especially numerous contributions of researcher Shingo Kubo at this center.

References

1) C. Kaido, T. Ogawa, Y. Arita, J. Yamasaki, and Y. Shishido: *J. Magn. Soc. Jpn.*, pp. 316-321, **31**, 4(2007) [in Japanese].
2) M. Gallaugher, N. Brodusch, R. Gauvin, and R. R. Chromik: *Ultramicroscopy*, pp. 40–49, 142(2014).
3) S. Szymura, C. Adamczyk, H. Majchrzak, J. Mehlis, and A. Zawada: *J. Mater. Sci. Lett.*, pp. 1259–1260, **6,** 11(1987).
4) K. C. Liao. *Metall. Trans. A*, pp. 1259– 1266, **17**, 8(1986).
5) H. Williams, R. Bozorth, and W. Shockley: *Phys. Rev.* pp. 155-178, **75**, 1(1949).
6) G. L. Houze: *J. Appl. Phys.,* pp. 1089-1096, **38**, 3(1967).
7) A. G. Tobin: *J. Appl. Phys.*, pp. 3611-3614, **40**, 9(1969).
8) J. Shilling and G. Houze: *IEEE Trans. Magn.*, pp. 195-223, **10**, 2(1974).
9) A. Morita, H. Fukui, H. Tadano, S. Hayashi, J. Hasegawa, and M. Niinomi: *Mater. Sci. Eng., A*, pp. 208-213, **280**, 1(2000).
10) K. Ono, T. Ogawa, and T. Sen: *Research paper of Industry Technology Center in Fukuoka,* pp. 99–103, 9(1999) [in Japanese].
11) T. Ogawa, Y. Ono, H. Koga, and K. Abiko: *Research paper of Industry Technology Center in Fukuoka*, 12(2001) [in Japanese].
12) F.J.G Landgraf, M Emura, J.C Teixeira, and M.F de Campos: *J. Magn. Magn. Mater.*, pp. 97-99, 215(2000)

Received Jul. 28, 2015; Revised Sep. 24, 2015; Accepted Oct. 22, 2015

J. Magn. Soc. Jpn., **40**, 13-17 (2016) <Paper>

Structure and Magnetic Properties of (001) Oriented CoPt-Ag and CoPd-Ag Alloy Films

T. Nagata, Y. Tokuoka, T. Kato, D. Oshima*, and S. Iwata*

Graduate School of Engineering, Nagoya University, *Furo-cho, Chikusa-ku, Nagoya 464–8603, Japan*

*EcoTopia Science Institute, Nagoya University, *Furo-cho, Chikusa-ku, Nagoya 464–8603, Japan*

20-nm-thick $(CoPt)_{100-x}Ag_x$ and $(CoPd)_{100-x}Ag_x$ (001) films (x = 0–20) were grown on MgO(001) substrate at a temperature of 300°C by molecular beam epitaxy, and their crystal structure and magnetic properties were compared with those of FePt-Ag and FePd-Ag films [Y. Tokuoka *et al.*: *J. Appl. Phys.*, **115**, 17B716 (2014)] for the systematic study of the effect of Ag addition into transition metal – noble metal alloy films. For the CoPt-Ag, the addition of 5% Ag increased perpendicular magnetic anisotropy (PMA) and coercivity. However, for the CoPd-Ag, Ag addition enhanced neither the PMA nor the coercivity. Structural analysis of the CoPt-Ag and CoPd-Ag films revealed that Ag addition promoted $L1_0$ phase ordering for CoPt-Ag, while $L1_0$ ordering was not found in CoPd-Ag. Although there were some similarities in the effect of Ag addition between CoPt-Ag and FePt-Ag, such as increased PMA, coercivity, and $L1_0$ ordering, there were different trends in PMA and $L1_0$ ordering between CoPd-Ag and FePd-Ag, except that both films showed reduced coercivity with Ag addition. Ag segregation and $L1_0$ ordering are considered important factors to explain the variations of structure and magnetic properties with Ag addition.

Key words: perpendicular magnetic anisotropy, Ag segregation, CoPt, CoPd

1. Introduction

Tetoragonal $L1_0$ phase magnetic materials, e.g., FePt and CoPt, have been extensively studied as potential candidates for future high-density perpendicular recording media because of their extremely large perpendicular magnetic anisotropies (PMA). However, for the practical application of these materials, there still remain challenges such as fabrication of nano-sized grains, control of (001) orientation, and lowering the ordering temperature of $L1_0$ phase[1), 2)]. One of the effective ways to realize these requirements is the addition of the third element. Ag or Cu addition into FePt is known to be effective to reduce its $L1_0$ ordering temperature[3)–6)]. The addition of Ag into CoPt is also known to promote $L1_0$ ordering and (001) orientation, which is crucial to obtain the large PMA[7), 8)]. Moreover, it is reported that the ordering temperature of FePd is reduced by insertion of the Ag underlayer[9)].

We have also studied FePt-Ag and FePd-Ag films to investigate the effect of Ag addition into $L1_0$ phase magnetic materials[10)–12)], and reported Ag addition to FePt with the amount of around 10 at. % is effective to promote $L1_0$ ordering and granular growth of FePt, resulting in the increase of the PMA and coercivity of the film normal direction. From the structural analysis and magnetic properties measurements, it was concluded that the Ag is segregated from FePt, and this phase separation promotes $L1_0$ ordering and granular growth of FePt[12)]. Unlike the case of FePt-Ag, Ag addition into FePd does not contribute to the corecivity increase and granular growth, and the formation of FePd-Ag alloy was observed[12)]. This suggests that the phase separation is a key factor to control the microstructure of $L1_0$ phase magnetic materials and to obtain suitable magnetic properties for the perpendicular recording media.

Recently, L. Zhang *et al.* reported that FePt-Ag:C films have large PMA and small grain size of around 6 nm[13)]. They reported a substantial increase of the PMA of FePt by the Ag addition, and the increase of the PMA is considered to be due to the phase separation of Ag and FePt by the heat treatment, in which the $L1_0$ ordering of FePt is promoted through the atom replacement by the Ag diffusion[14)].

In this paper, CoPt-Ag and CoPd-Ag films have been studied in detail for the systematic understanding of the effect of Ag addition in 3*d* transition metal and noble metal alloy films. Although no ordered phase is reported in bulk CoPd[15)], metastable $L1_0$ phase CoPd was reported in evaporated CoPd alloy films[16)]. The phase separation of Ag and CoPt or CoPd as well as the enhancement of $L1_0$ ordering by Ag addition are discussed. In addition to the structural analysis, the relationship between the structure and magnetic properties is studied in detail. Furthermore, the effect of Ag addition into CoPt and CoPd is compared with the results of previously reported FePt-Ag and FePd-Ag.

2. Experiment

In our previous study, 5 nm-thick $(FePt)_{100-x}Ag_x$ and $(FePd)_{100-x}Ag_x$ were grown directly on MgO(001) substrates[12)]. However, *c*–axis orientation of 5 nm-thick CoPt on MgO(001) was poor compared to the FePt-Ag, due to the lattice mismatch between CoPt and MgO. Thus in this study, 20 nm-thick $(CoPt)_{100-x}Ag_x$ and $(CoPd)_{100-x}Ag_x$ films (x = 0–20) were grown by molecular beam epitaxy (MBE) method. The CoPt-Ag was grown directly on MgO(001) substrates while CoPd-Ag was

grown on 10 nm thick Pd (001) buffer layer to reduce the lattice mismatching between CoPd and MgO(001) substrate. The Pd buffer layer was grown at room temperature, and CoPt and CoPd layers were grown at 300°C. Co, Pt (Pd), and Ag were co-evaporated from independently controlled e-beam sources, for which the deposition rate of each element was monitored by quartz thickness monitors. During the deposition, the MBE chamber was kept at a pressure of less than 3×10^{-7} Pa. Before the deposition, the MgO substrate was cleaned by 1 keV Ar^+ ion bombardment followed by the heat treatment at 1000°C in the MBE chamber.

The film structure was characterized by *in-situ* reflection high energy electron diffraction (RHEED) and *ex-situ* X-ray diffraction (XRD) using Cu $K\alpha$ radiation source (λ = 0.15418 nm). Hysteresis loops and magnetic anisotropies were measured by an alternating gradient field magnetometer and a torque magnetometer, respectively. The surface topography was checked by the atomic force microscopy (AFM).

3. Results and Discussions

3.1 Crystal structure and surface morphology

Figure 1 shows ω–2θ XRD profiles of $(CoPt)_{100-x}Ag_x$ and $(CoPd)_{100-x}Ag_x$ grown at 300°C. In the profiles of CoPt-Ag, 001 superlattice and 002 fundamental diffractions were clearly seen, which indicates the existence of (001) oriented $L1_0$ phase. Moreover, CoPt 001 peak intensity increased by adding Ag and no significant changes in the peak positions of CoPt 001 and 002 with the Ag addition were found. In the profiles of CoPd-Ag, Pd 002 and CoPd 002 peaks indicate the (001) oriented growth of Pd buffer and CoPd layers on the MgO(001) substrate. At x = 0, there exist reflections indicated as "*" in the figure around 2θ = 16 deg and 32 deg. The lattice spacings estimated from these peaks are 0.55 nm and 0.28 nm, respectively, which coincide with 3- and 1.5-times of CoPd 002 spacing of 0.184 nm. This suggests the existence of the long range order structure along the CoPd [001] direction. With the increase of Ag content, this long range order structure of CoPd disappeared. The lattice constant estimated from the CoPd 002 was 0.366 nm, and the peak position of CoPd 002 did not change significantly with increasing Ag content.

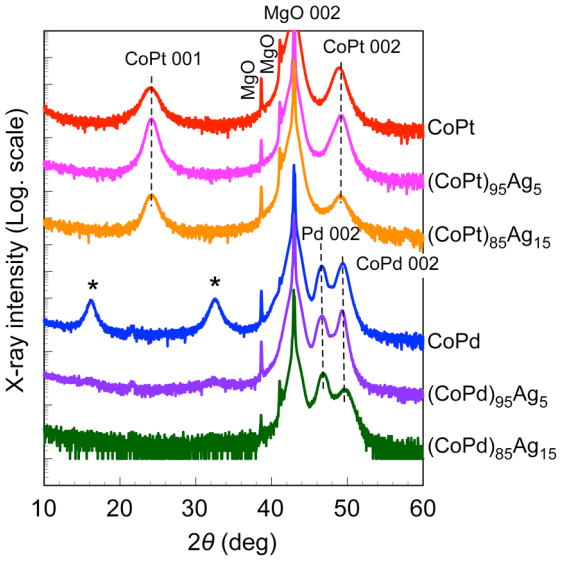

Fig. 1 ω–2θ XRD profiles of $(CoPt)_{100-x}Ag_x$ and $(CoPd)_{100-x}Ag_x$ alloy films (x = 0, 5, and 15) grown at 300°C. X-ray scattering vector is normal to the film surface. For the profile of CoPd, there exist reflections indicated as "*" around 2θ = 16 deg and 32 deg. The lattice spacings estimated from these peaks are 0.55 nm and 0.28 nm, respectively, which coincide with 3- and 1.5-times of CoPd 002 spacing of 0.184 nm.

The reciprocal space mapping of CoPd also showed the existence of the long range order structure along [001] direction. Figure 2 shows the reciprocal space mapping for a slice of (110) plane of CoPd grown on MgO (001) at 300°C. The Q_x and Q_z are along MgO[110] and [001] directions, respectively, and the radial component of the scattering vector was calculated as:

$$\sqrt{Q_x^2 + Q_z^2} = \frac{2\sin\theta}{\lambda}, \qquad (1)$$

where λ = 1.5418 Å and θ is Bragg angle.

The diffraction spots at Q_z = 0.18 $Å^{-1}$ and 0.36 $Å^{-1}$ correspond to the peaks indicated as "*" in Fig. 1. Besides these spots, several diffraction spots, such as (Q_x, Q_z) = (–0.37 $Å^{-1}$, 0.63 $Å^{-1}$) and (0.37 $Å^{-1}$, 0.63 $Å^{-1}$) are seen, suggesting the existence of the long range order structure along CoPd [001] direction. More detail structural analysis is necessary to elucidate the

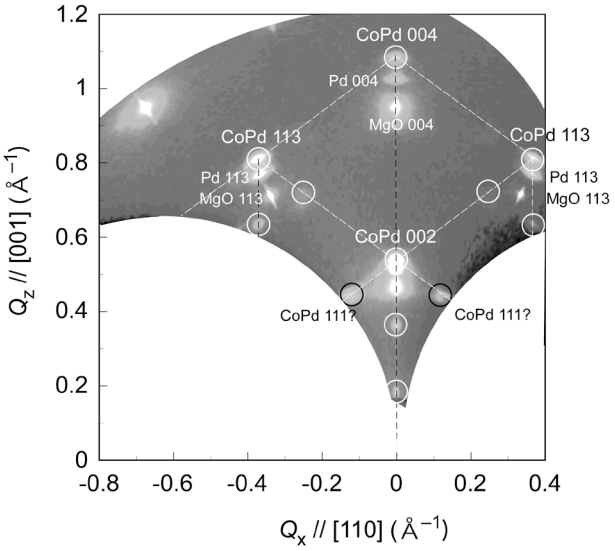

Fig. 2 Reciprocal space mapping of (110) plane of CoPd film grown on MgO (001) at 300°C.

structure of CoPd alloy films, but at present we consider two possibilities: atomic layered structure along [001] direction with a period of 3 times of 002 spacing (0.184 nm) or periodic anti-phase domain boundary similar to that observed in CuAu[17], Cu_3Pd[18], etc.

Figure 3 shows in-plane ϕ–$2\theta\chi$ XRD profiles of $(CoPt)_{100-x}Ag_x$ and $(CoPd)_{100-x}Ag_x$ with x = 0 and 15. The profiles were taken under the condition that the X-ray scattering vector is along MgO [100] direction. Besides the reflection of MgO 200, intense peak from CoPt 200 or CoPd 200 is seen in the profile at x = 0. No superlattice reflections of CoPt and CoPd were seen in the profiles. The addition of Ag did not significantly change the peak position of CoPt 200 and CoPd 200, and Ag 200 peak was seen in the profiles at x = 15. The lattice constants a estimated from the CoPt 200 and CoPd 200 peaks were 0.380 nm and 0.379 nm, respectively. From these structural analyses, we concluded that the Ag is segregated from CoPt or CoPd, and promotes $L1_0$ ordering of CoPt. $L1_0$-CoPt is well known as a stable phase near equiatomic composition of Co and Pt, while $L1_0$-CoPd is reported to be metastable[16]. Although, the addition of the third element, e.g., C, was reported to stabilize the metastable $L1_0$-MnAl phase in the Mn-Al system[19], the Ag addition to Co-Pd seems to have no significant effect to obtain metastable $L1_0$-CoPd phase.

Figure 4 shows the RHEED patterns of $(CoPt)_{100-x}Ag_x$ with Ag amount of x = 0–15. The incidence of the electron beam was along [100] direction of MgO(001) substrate and the patterns were taken after the deposition of CoPt-Ag films. For x = 0, streak patterns with a space corresponding to the in-plane lattice spacing of CoPt were observed. The "vertical" streak pattern means slightly broadened reciprocal

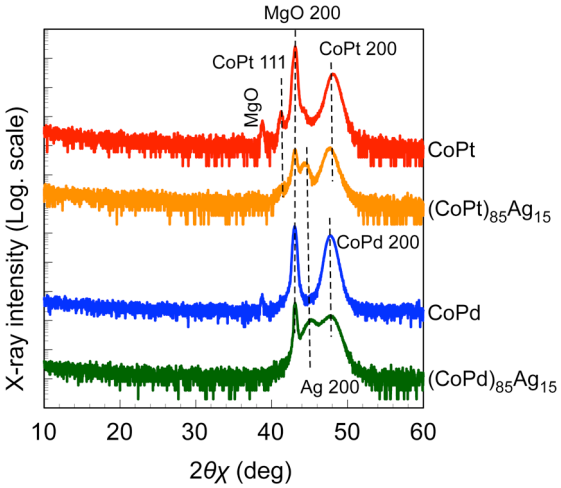

Fig. 3 In-plane ϕ–$2\theta\chi$ XRD profiles of $(CoPt)_{100-x}Ag_x$ and $(CoPd)_{100-x}Ag_x$ alloy films (x = 0 and 15) grown at 300°C. X-ray scattering vector is parallel to MgO [100] direction.

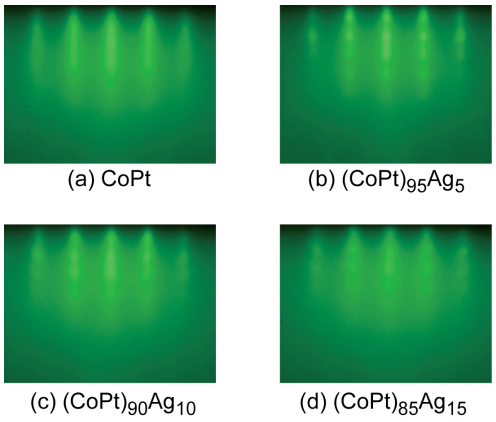

Fig. 4 RHEED patterns of $(CoPt)_{100-x}Ag_x$ grown at 300°C with Ag amounts of (a) x = 0, (b) 5, (c) 10, and (d) 15. The incidence of electron beam was along [100] direction of MgO(001) substrate. All patterns were taken after deposition of CoPt-Ag films.

lattice rods of CoPt, indicating rather flat surface of CoPt with atomic steps. With increasing the Ag content, the RHEED pattern changed from streaks to vertically aligned spots. This means the incident electrons passed inside the CoPt crystals, and thus indicates the granular growth of the CoPt-Ag. The AFM images of $(CoPt)_{95}Ag_5$ and $(CoPt)_{85}Ag_{15}$ are shown in Figs. 5 (a) and (b), respectively. With increasing the Ag content, the granular growth of the CoPt-Ag was confirmed, which coincides well with the RHEED observation. A similar granular growth by the addition of Ag was also confirmed in CoPd-Ag films. The granular structures of CoPt-Ag and CoPd-Ag are considered to be induced by the segregation of Ag from CoPt or CoPd, and we consider the Ag covers CoPt or CoPd grains, forming core/shell structure as observed in the FePt-Ag:C film[14]. White protrusions in Fig. 5 (b) are quite similar to Ag re-precipitates at the top of the FePt-oxide film reported by Yang *et al.*[20]. In such case, the actual Ag content in

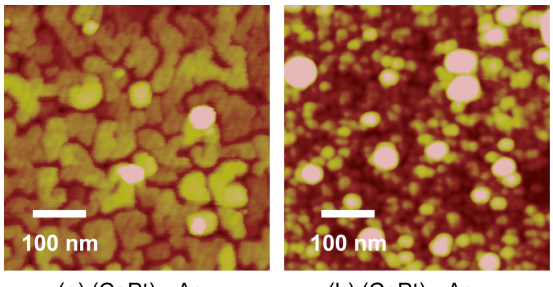

Fig. 5 AFM images of $(CoPt)_{95}Ag_5$ and $(CoPt)_{85}Ag_{15}$ grown at 300°C. Image area is 500 nm × 500 nm and vertical scale of image is 20 nm. Mean roughness R_a of image is (a) 1.47 nm and (b) 2.26 nm.

the CoPt-Ag may be smaller than the designed value. A similar granular growth by the addition of Ag was also confirmed in CoPd-Ag films.

3.2 Magnetic properties

The structural variations of CoPt-Ag and CoPd-Ag strongly affect their magnetic properties. Figure 6 shows hysteresis loops of $(CoPt)_{100-x}Ag_x$ and $(CoPd)_{100-x}Ag_x$, where the external field was applied parallel and perpendicular to the film plane. Figure 7 shows the Ag content dependence of the PMA, K_u, of CoPt-Ag and CoPd-Ag films, where the K_u was estimated from the torque curve applying a magnetic field of 15 kOe. For comparison, the K_u of the previously reported FePt-Ag and FePd-Ag are also shown in the same figure. For the CoPt-Ag, the increases of PMA and coercivity were found by the addition of Ag with an amount of 5 at. % as shown in Fig. 6 (b) and Fig. 7. However, for the CoPd-Ag, Ag addition reduced the PMA (see Fig. 7) and did not contribute to enhance the coercivity as shown in Fig. 6 (d)–(f). Interestingly, the CoPd film has some PMA and coercivity, which may be related to the long range order structure along CoPd [001] direction as discussed in Fig. 2. The variations of the magnetic properties of CoPt and CoPd with Ag content will be explained by the structural variation. For CoPt-Ag, Ag addition promotes $L1_0$ ordering, and Ag

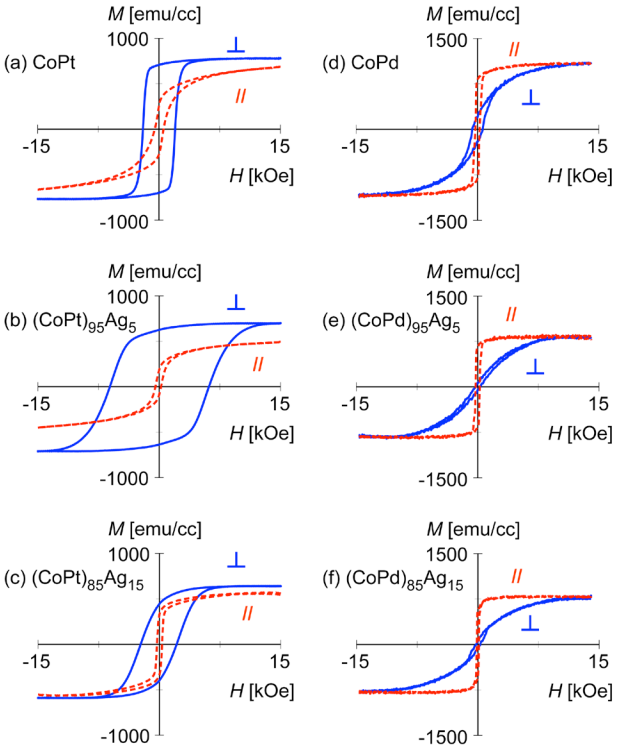

Fig. 6 Hysteresis loops of (a)–(c) $(CoPt)_{100-x}Ag_x$ and (d)–(f) $(CoPd)_{100-x}Ag_x$, where the external field was applied parallel and perpendicular to the film plane. Ag contents are (a), (d) x = 0, (b), (e) x = 5, and (c), (f) x =15.

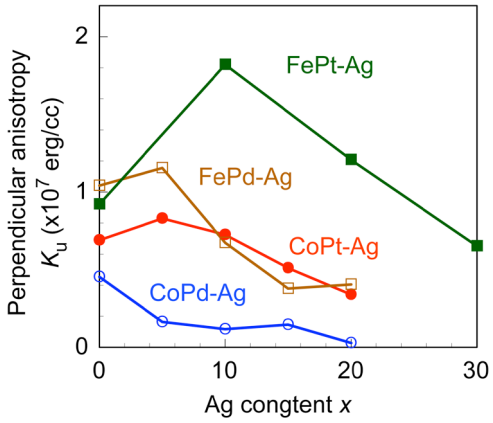

Fig. 7 Ag content dependence of perpendicular anisotropy K_u of CoPt-Ag and CoPd-Ag films, where K_u was estimated from torque curve applying a magnetic field of 15 kOe. For comparison, the K_u of the previously reported FePt-Ag grown at 250°C and FePd-Ag grown at 400°C are also shown[12].

atoms are considered to segregate from CoPt, which will make the $L1_0$-CoPt grains smaller as observed in Figs. 4 and 5. These structural variations will increase the PMA and coercivity of the CoPt-Ag films. On the other hand, Ag did not assist the formation of the $L1_0$ phase CoPd, which does not contribute to enhance the PMA and coercivity even though the granular growth was promoted by the Ag addition.

By comparing these results with those of the previously reported FePt-Ag and FePd-Ag[12], we found a similarity between FePt-Ag and CoPt-Ag. For both alloys, Ag addition enhanced their PMA and coercivity as shown in Fig. 7 and Ref. 12), owing that the Ag addition promoted the $L1_0$ ordering and granular growth. Also, there exists a similarity between FePd-Ag and CoPd-Ag; Ag addition did not contribute to enhance the coercivity in both alloys. However, there is a difference between FePd-Ag and CoPd-Ag. For FePd-Ag, the Ag tend to form an alloy with FePd, which lowers the coercivity even though its PMA slightly increases with the Ag addition of 5 at. % due to the increase of $L1_0$ ordering. For CoPd-Ag, the Ag atoms segregate from the CoPd, which makes the grains smaller, but the Ag does not contribute to promote $L1_0$ ordering.

4. Conclusion

The effect of Ag addition to CoPt and CoPd on their crystal structures and magnetic properties was investigated, and the results were compared with those of previously reported FePt-Ag and FePd-Ag for the systematic understanding of the effect of the Ag addition. It was confirmed that Ag atoms in the CoPt segregate from CoPt, which promotes $L1_0$ ordering and granular growth of CoPt. Such structural variations improved the magnetic properties of CoPt for a

perpendicular recording medium, e.g., increases of PMA and coercivity. These tendencies were similar to the results of FePt-Ag, in which Ag segregation effectively increases PMA and coercivity of FePt. On the other hand, Ag addition does not contribute to the increase of coercivity of CoPd, which is similar to the result of FePd-Ag. However, the microstructure of CoPd-Ag is different from that of FePd-Ag. For CoPd-Ag, Ag atoms segregate from CoPd, but do not assist the formation of the $L1_0$ CoPd phase. On the other hand, for FePd-Ag, Ag tends to form an alloy with FePd, which slightly promote the $L1_0$ ordering of FePd but does not contribute to the granular growth. From these results, it is considered that the reason why Ag is an effective material to obtain high ordered $L1_0$ phase and small sized grains is a low solubility of Ag to FePt and CoPt as well as a low surface energy of Ag, which will be effective to make core/shell structure as reported in Ref. 14).

Acknowledgements The authors would like to thank Mr. M. Kumazawa of Nagoya University for his assistance in the experiments. The authors are grateful for the financial support by Grant-in-Aids for Scientific Research from the Ministry of Education, Culture, Sports, Science and Technology.

References

1) P. Lu and S. H. Charap: *IEEE Trans. Magn.*, **31**, 2767 (1995).
2) D. Weller, A. Moser, L. Folks, M. E. Best, W. Lee, M. F. Toney, M. Schwickert, J. U. Thiele, and M. F. Doerner: *IEEE Trans. Magn.*, **36**, 10 (2000).
3) T. Maeda, T. Kai, A. Kikitsu, T. Nagase, and J. Akiyama: *Appl. Phys. Lett.*, **80**, 2147 (2002).
4) C. L. Platt, K. W. Wierman, E. B. Svedberg, R. Veerdonk, J. K. Howard, A. G. Roy, and D. E. Laughlin: *J. Appl. Phys.*, **92**, 6104 (2002).
5) K. Kang, T. Yang, and T. Suzuki: *IEEE Trans. Magn.*, **38**, 2039 (2002).
6) Y. Shao, M. L. Yan, and D. J. Sellmyer: *J. Appl. Phys.*, **93**, 8152 (2003).
7) C. Chen, O. Kitakami, S. Okamoto, and Y. Shimada: *Appl. Phys. Lett.*, **76**, 3218 (2000).
8) V. Karanasos, I. Panagiotopoulos, D. Niarchos, H. Okumura, and G. C. Hadjipanayis: *Appl. Phys. Lett.*, **79**, 1255 (2001).
9) B. Li, W. Liu, X. G. Zhao, S. Ma, W. J. Gong, J. N. Feng, F. Wang, and Z. D. Zhang: *Mater. Lett.*, **100**, 58 (2013).
10) T. Konagai, Y. Kitahara, T. Itoh, T. Kato, S. Iwata, and S. Tsunashima: *J. Magn. Magn. Mater.*, **310**, 2662 (2007).
11) R. Ikeda, M. Kagami, T. Kato, S. Iwata, and S. Tsunashima: *J. Magn. Soc. Jpn.*, **33**, 493 (2009).
12) Y. Tokuoka, Y. Seto, T. Kato, and S. Iwata: *J. Appl. Phys.*, **115**, 17B716 (2014).
13) L. Zhang, Y. K. Takahashi, K. Hono, B. C. Stipe, J. -Y. Juang, and M. Grobis: *J. Appl. Phys.*, **109**, 07B703 (2011).
14) B. S. D. Ch. S. Varaprasad, Y. K. Takahashi, J. Wang, T. Ina, T. Nakamura, W. Ueno, K. Nitta, T. Uruga, and K. Hono: *Appl. Phys. Lett.*, **104**, 222403 (2014).
15) K. Ishida and T. Nishizawa, *Binary Alloy Phase Diagrams*, 2nd ed., vol. 2, (ASM International, 1990), pp. 1220–1223.
16) Y. Matsuo: *J. Phys. Soc. Jpn.*, **32**, 972 (1972).
17) S. Ogawa and D. Watanabe: *J. Phys. Soc. Jpn.*, **9**, 475 (1954).
18) D. Watanabe, S. Ogawa: *J. Phys. Soc. Jpn.*, **11**, 226 (1956).
19) W. H. Dreizler and A. Menth: *IEEE Trans. Magn.*, **MAG-16**, 534 (1980).
20) E. Yang, D. E. Laughlin, J. G. Zhu: *IEEE Trans. Magn.*, **46**, 2446 (2010).

Received Jul. 27, 2015; Accepted Oct. 28, 2015

日本磁気学会　第 206 回研究会

発電用電子・磁気材料の現状と今後の展望

地球温暖化の抑制と温室効果ガス排出量削減するために化石資源に代わるエネルギー源の有効活用の必要性が高まっています．中でも，近年，環境からの微小なエネルギーを電力に変換する技術の研究が精力的に行われています．本研究会では発電用電子・磁気材料に着目し，振動発電，熱電変換，磁気冷凍について第一線でご活躍されている6名の研究者の方を講師としてお招きし，ご講演いただきます．発電用電子・磁気材料の現状と今後の展望について活発に議論していただけます．多くの方のご参加をお待ちしております．

日時: 2016 年 1 月 29 日（金）13:00～16:45

場所: 中央大学駿河台記念館　330 号室　（東京都千代田区神田駿河台 3-11-5）
TEL：03-3292-3111　（記念館事務室）
URL：http://www.chuo-u.ac.jp/access/surugadai/

参加費: 無料（研究会資料予約購読者，学生）
2,000 円（会員，協賛会員）
4,000 円（非会員）

資料代: 1,000 円（会員，協賛会員，非会員，学生）

協賛: IEEE MAG-33 Sendai/Tokyo/Shin-Etsu/Nagoya/Kansai/Fukuoka Chapters，応用物理学会，電気学会，日本金属学会，日本熱電学会，低温工学・超電導学会，日本磁気科学会，エネルギーハーベスティングコンソーシアム

問い合わせ先: 日本磁気学会事務局　TEL：03-5281-0106
URL：http://www.magnetics.jp/event/research/topical_206/

オーガナイザ: 東　大地（日立金属）、小山恵史（大同特殊鋼）、関　剛斎（東北大）

プログラム

座長：東　大地（日立金属）

13:00 - 13:35　「エナジーハーベスティング技術の現状と将来」
○竹内敬治（NTT データ経営研究所）

13:35 - 14:10　「磁歪式振動発電を用いたバッテリーフリーIoT の実用化展開」
○上野敏幸（金沢大）

14:10 - 14:45　「積層同時焼成磁気回路を用いた MEMS マイクロエアタービンの開発」
○内木場文男（日大）

休憩（15 分）

座長：関　剛斎（東北大）

15:00 - 15:35　「エレクトレット振動発電器のマーケット調査」
○諸口　登（小西安）

15:35 - 16:10　「異常ネルンスト効果を利用した環境発電素子のための磁性材料開発とその展望」
○桜庭裕弥（物材機構）

16:10 - 16:45　「磁気と熱のエネルギー変換機能磁性材料とその応用」
○斉藤明子（東芝）

当学会では，研究会でのビデオ・写真撮影および録音はご遠慮いただいております．

The 206th Topical Symposium of the Magnetic Society of Japan

Present Status and Prospects of Electronic and Magnetic Materials for Power Generation

Use of energy sources except fossil fuels becomes more important to reduce green house gas emission. In the past few years there have been extensive efforts to investigate the power generation by using small amount of energy from the environment. In this symposium, six lecturers will give recent trends and prospects of electronic and magnetic materials for vibrational power generator, thermoelectric conversion, magnetic refrigeration etc. We welcome the participation of all of you.

INFORMATION

Date:	January 29th (Friday), 2016 13:00 - 16:45
Venue:	Room 330, Surugadai Memorial Hall, Chuo University (3-11-5 Kanda-Surugadai, Chiyoda-ku, Tokyo) Tel: 03-3292-3111 URL: http://global.chuo-u.ac.jp/english/siteinfo/visit/surugadai/
Admission Fee:	Free (reserved readers and students) 2,000 Yen (members and corporate members) 4,000 Yen (non-members)
Booklet:	1,000 Yen (members, corporate members, non-members and students)
In cooperation with:	IEEE MAG-33 Sendai/Tokyo/Shin-Etsu/Nagoya/Kansai/Fukuoka Chapters, The Japan Society of Applied Physics, The Institute of Electrical Engineers of Japan, The Japan Institute of Metals and Materials, The Thermoelectrics Society of Japan, Cryogenics and Superconductivity Society of Japan, The Magneto-Science Society of Japan, Energy Harvesting Consortium
Information:	The Magnetic Society of Japan / Tel: 03-5281-0106 URL: http://www.magnetics.jp/archive/english/seminar/206.html
Organizers:	Daichi Azuma (Hitachi Metals), Shigenobu Koyama (Daido Steel), Takeshi Seki (Tohoku Univ.)

Program

Chair: D .Azuma (Hitachi Metals)

13:00 - 13:35 “Current status and prospects of energy harvesting technologies”
○K. Takeuchi (NTT DATA INSTITUTE OF MANAGEMENT CONSULTING)

13:35 - 14:10 “Practical applications of battery free IoT using magnetostrictive vibrational power generator”
○T. Ueno (Kanazawa Univ.)

14:10 - 14:45 “Development of MEMS micro air turbine generator with multilayer Co-fired magnetic circuit”
○F. Uchikoba (Nihon Univ.)

Break (15 min.)

Chair: T. Seki (Tohoku. Univ.)

15:00 - 15:35 “Market research for electret vibration energy harvester”
○N. Moroguchi (Konishiyasu)

15:35 - 16:10 “Development of the magnetic materials for energy harvesting devices using anomalous Nernst effect and its prospect”
○Y. Sakuraba (NIMS)

16:10 - 16:45 “Magnetic materials for thermal and magnetic energy conversion and application to refrigeration”
○A. Saito (Toshiba)

The presentations will be given in Japanese. / Audio and/or visual recording is prohibited.

Journal of the Magnetics Society of Japan

Vol. 40 No. 1 (通巻第 283 号) 2016 年 1 月 1 日発行

Vol. 40 No. 1 Published January 1, 2016
by the Magnetics Society of Japan
5F Mitsui Sumitomo Kaijo Ogawamachi Bldg. 2–8, Kanda Ogawamachi, Chiyoda-ku, Tokyo 101–0052
Tel. +81–3–5281–0106 Fax. +81–3–5281–0107

Printed by JP Corporation Co., Ltd.
2–3–36, Minamikase, Saiwai-ku, Kanagawa 212–0055
Advertising agency: Kagaku Gijutsu-sha

発行：（公社）日本磁気学会 101–0052 東京都千代田区神田小川町 2–8 三井住友海上小川町ビル 5 階
製本：（株）ジェイピーコーポレーション 212–0055 神奈川県川崎市幸区南加瀬 2–3–36 Tel.（044）571–5815
広告取扱い：科学技術社 111–0052 東京都台東区柳橋 2–10–8 武田ビル 4F Tel.（03）5809–1132